Mixing of passive scalars in viscoelastic turbulent jets and wakes

Mateus C. Guimarães,[1,*] Fernando T. Pinho,[2,3] and Carlos B. da Silva[1,†]
[1]IDMEC/LAETA, Instituto Superior Técnico, Universidade de Lisboa, 1049-001 Lisboa, Portugal
[2]ALiCE, Faculdade de Engenharia, Universidade do Porto, 4200-465 Porto, Portugal
[3]CEFT, Faculdade de Engenharia, Universidade do Porto, 4200-465 Porto, Portugal

(Received 9 January 2023; accepted 23 January 2025; published 18 February 2025)

Direct numerical simulations (DNSs) of spatially evolving turbulent planar jets and wakes of viscoelastic polymer solutions are performed in order to study the small-scale mixing and large-scale stirring of passive scalars in free turbulent viscoelastic flows. The finitely extensible nonlinear elastic–Peterlin rheological model is adopted for the DNS. Viscoelasticity is found to suppress small-scale scalar mixing but it initially suppresses and later enhances large- and intermediate-scale stirring, provided viscoelasticity is sufficiently high. The normalized dissipation rate of scalar variance that is typically used to quantify the small-scale mixing is reduced by a factor larger than 4 in some cases, whereas the normalized turbulent flux, which is characteristic of the large-scale stirring, increases by a factor larger than 6 in the most significant case. The explanation is the suppression of small-scale perturbations caused by the polymers, suppressing the mixing, and allowing the appearance of larger coherent structures that promote the stirring at the large scales. In the high elasticity region, the transport of passive scalars is more strongly modified by viscoelasticity than the momentum transport, and the Reynolds analogy is not applicable.

DOI: 10.1103/PhysRevFluids.10.023303

I. INTRODUCTION

The addition of long-chain polymers to a Newtonian solvent can have a substantial influence on the dynamics of a turbulent scalar field. A problem of considerable practical interest is the transport of heat over long distances, as in large district heating and cooling systems [1,2], where the temperature field can be considered a passive scalar provided its variations are not too large and thermodynamic and transport fluid properties are approximately constant.

Scalar transport has been computed by direct numerical simulations (DNSs) of viscoelastic turbulent flows between parallel plates [3,4], flat plate boundary layers [5], cylinder wakes [6] and temporally evolving shear layers [7]. These studies confirmed the strong influence of viscoelasticity on the scalar transport that had already been documented in previous experimental works [1]. In particular, turbulent heat transfer reduction of up to 90% has been reported in fully developed pipe flow.

The first DNS of turbulent viscoelastic jets has been performed only recently, by Guimarães *et al.* [8]. The work focused on the velocity and conformation field statistics and the development of a theory for the far-field fully turbulent region at high Reynolds numbers, which was later extended to small velocity deficit planar wakes in Guimarães *et al.* [9], and to different polymer deformation regimes in Guimarães *et al.* [10].

*Present address: DCS Computing GmbH, Industriezeile 35, Linz 4020, Austria.
†Contact author: carlos.silva@tecnico.ulisboa.pt

It was found that when the inlet Weissenberg number Wi is sufficiently high there is a strong attenuation of the viscous dissipation rate, resulting in a large reduction of the spreading and decay rates of the shear layer [8,11], and a suppression of turbulent velocity fluctuations. However, when the local Deborah number is low, the opposite effect is observed and there is a moderate enhancement of turbulent velocity fluctuations and spreading rates. Thus, the far field of high Wi turbulent jets and wakes is composed of two distinct regions: the high elasticity region and the low elasticity region [9].

A similar behavior was observed more recently, in experiments involving turbulent round jets with polyethylene oxide (PEO) solutions [12]. Considering turbulent planar jets of PEO, the self-similar evolution of the flow predicted by Guimarães *et al.* [8] was confirmed in the experiments of Yamani *et al.* [11], who also studied the evolution of inertioelastic instabilities in the transition region of the jet. Yamani *et al.* [11] found that, in the transition region, two different elasticity regimes also exist, where the effect of the polymers is nonmonotonic and can either destabilize or stabilize the perturbations, in agreement with previous linear stability analysis [13], and a more recent DNS study [14]. In the fully turbulent region at the high elasticity regime, the turbulent energy spectrum has a -3 power-law exponent that is different from the classical $-5/3$ law of Newtonian turbulence [9,11,15–17].

The physical mechanisms responsible for the modifications of the spreading rate of viscoelastic shear layers were elucidated in Abreu *et al.* [18], using a fully resolved DNS of turbulent/nonturbulent interfaces (TNTIs) at high Reynolds numbers. At high Weissenberg numbers (Wi), the enhancement of the turbulent entrainment velocity caused by viscoelasticity is countered by a substantial decrease of the surface area and fractal dimension of the irrotational boundary, resulting in a suppression of the entrainment rate and therefore a decrease of the spreading rate of the shear layers.

Analyzing the budgets of vorticity magnitude at the TNTI, Abreu *et al.* [18] recognized the viscoelastic production term as the dominant term contributing to the decrease of the turbulent entrainment at high Wi. In fact, this term, which is absent in Newtonian shear layers, can be interpreted as a polymer torque and is the main ingredient of a mechanism proposed by Kim *et al.* [19] to explain polymer-induced turbulent drag reduction in wall flows. It can be a sink or a source of vorticity, but in fully turbulent flows at high Wi it is predominantly a dissipation term, i.e., a counterrotating polymer torque suppressing the small-scale vorticity and deforming the vortex structures, that assume the shape of thin vortex sheets, instead of tubes [18–21].

The polymer torque also plays an important role in the transition regime, as demonstrated by Page and Zaki [22] using nonmodal linear stability analysis. However, in contrast with the fully turbulent regime, the transitioning shear layer is destabilized by polymer torque perturbations, i.e., in this case the polymer torque perturbations contribute to the growth of vorticity perturbations. This was corroborated by the DNS results of Guimarães *et al.* [14], who also extended the analysis to the nonlinear regime of perturbation growth.

The suppression of small-scale turbulent fluctuations in viscoelastic jets that was observed by Guimarães *et al.* [8] and Yamani *et al.* [11] was already documented in the earliest experimental studies of turbulent viscoelastic jets, using flow visualization techniques [23–32]. However, considering the measurements of the velocity field, some authors of these early studies believed that the inconsistencies observed between the different data sets, concerning whether viscoelasticity increases or decreases Reynolds stresses and spreading and decay rates, was a result of experimental error, and that the results were contradictory. Indeed, some of those measurements were obtained by intrusive methods, such as Pitot tubes or hot-film anemometers [33–37] that are inadequate for viscoelastic flows, but the differences persisted even when proper nonintrusive techniques, such as the laser Doppler anemometer, were employed [31,38–41].

In light of the newest works on viscoelastic jets, using fully resolved numerical simulations [8–10,14], modern experimental techniques [11,12,17] and analytical tools [8–10,13,22], it is clear that the inconsistencies between those earlier experimental works are not contradictory, but the result of the complex and rich dynamics of polymer solutions. Since the polymers will cause, e.g., a decrease or increase of velocity and vorticity fluctuations, with a nonmonotonic evolution, depending on the flow regime (linear or nonlinear transition or fully developed turbulence), local values of the Weissenberg number, polymer concentration, and molecular weight, it is crucial to know in detail the rheology of the polymer solutions in order to draw conclusions about viscoelastic effects at a particular flow regime.

Additionally, thanks to these recent numerical, experimental, and analytical investigations our understanding of the physics of free turbulent shear layer flows with dilute polymer solutions has reached some level of maturity. However, these efforts have focused mainly on the velocity and vorticity fields, and it is currently unknown how viscoelasticity affects the evolution of a passive scalar field in free turbulent jets and wakes at high Reynolds numbers. Given the strong influence of polymers on the dynamics of a turbulent scalar field near a solid wall [1,3–5], it is expected that free shear flows such as jets and wakes will also be dramatically modified by viscoelasticity, but even the most fundamental turbulence statistics, such as the passive scalar spreading and decay rates, have not yet been measured or evaluated.

Here we focus on the mixing and stirring of passive scalars in the fully turbulent far-field region of planar jets and wakes of viscoelastic polymer solutions over a wide range of viscoelasticity conditions. Using a new DNS database that employs computational domains that are much larger than those considered before [8,9,14], we assess the influence of viscoelasticity on the classical turbulence statistics of the passive scalar at the different elasticity regimes, and show how the results can be explained by evaluating the effect of the polymers on the flow structure at both small and large scales of motion.

This paper is organized as follows. The numerical methods and physical parameters of the DNS are discussed in Sec. II. The evolution and mixing of passive scalars are analyzed and explained in Sec. III, its description is complemented by budgets of passive scalar variance in Sec. IV, and some conclusions are drawn in Sec. V. In order to improve the readability of the paper, some demonstrations and supplementary results are shown in the Appendixes.

II. DIRECT NUMERICAL SIMULATIONS

A. Governing equations

To characterize the rheology of the long-chain dilute and semidilute polymer solutions we use the Finitely Extensible NonLinear Elastic constitutive model closed with Peterlin's approximation, i.e., the FENE-P model of Bird *et al.* [42], but in a slightly modified format due to Sureshkumar *et al.* [43]. The momentum equation is

$$\frac{\partial \boldsymbol{u}}{\partial t} + \boldsymbol{u} \cdot \nabla \boldsymbol{u} = -\frac{1}{\rho}\nabla p + \nu^{[s]}\nabla^2 \boldsymbol{u} + \frac{1}{\rho}\nabla \cdot \boldsymbol{\sigma}^{[p]}, \tag{1}$$

where the polymer stress tensor is

$$\boldsymbol{\sigma}^{[p]} = \frac{\rho \nu^{[p]}}{\tau_p}[f(C_{kk})\boldsymbol{C} - \boldsymbol{I}], \tag{2}$$

and the equation for the conformation tensor $\boldsymbol{C}$ is given by

$$\frac{\partial \boldsymbol{C}}{\partial t} + \boldsymbol{u} \cdot \nabla \boldsymbol{C} = \nabla \boldsymbol{u}^T \cdot \boldsymbol{C} + \boldsymbol{C} \cdot \nabla \boldsymbol{u} - \frac{1}{\tau_p}[f(C_{kk})\boldsymbol{C} - \boldsymbol{I}]. \tag{3}$$

The Peterlin function used in the present work is given by $f(C_{kk}) \equiv (L^2 - 3)/(L^2 - C_{kk})$ and the fluid incompressibility condition is imposed by the continuity equation

$$\nabla \cdot \boldsymbol{u} = 0. \tag{4}$$

The polymer relaxation time is τ_p, the polymer and solvent zero-shear kinematic viscosities are $\nu^{[p]}$ and $\nu^{[s]}$, respectively, and L is the maximum length of the fully extended polymer dumbbells normalized by their equilibrium radius. The ratio of zero shear rate viscosities is $\beta = \nu^{[s]}/(\nu^{[s]} +$

$\nu^{[p]}$). For dilute polymer solutions the polymer concentration is approximately proportional to $1-\beta$ and therefore we call $1-\beta$ the polymer concentration parameter.

The evolution equation for the passive scalar field θ is given by the advection-diffusion equation,

$$\frac{\partial \theta}{\partial t} + \boldsymbol{u} \cdot \nabla \theta = D \nabla^2 \theta, \tag{5}$$

where D is the diffusivity coefficient of θ. As mentioned in the Introduction, the passive scalar θ can be considered, e.g., the temperature field, provided temperature variations are not too large, or the concentration of injected dye that is typically used to visualize flow structures in experiments.

B. Numerical methods

The computational code and numerical methods used for the solution of momentum, mass, scalar, and conformation tensor equations have been described in detail elsewhere (Guimarães *et al.* [8]; da Silva *et al.* [44]) and so only a brief description will be given here. Validation studies of the code can also be found in previous references [8,9,14,44–46] and some additional validation that is complementary to those studies is also provided in Appendix D.

The momentum equation is solved with highly accurate pseudospectral combined with sixth-order compact finite difference schemes [47,48], while an explicit third-order Runge-Kutta scheme is used for time advancement [49] and the pressure-velocity coupling is treated with the fractional step method of Kim and Moin [50]. Inflow and outflow boundary conditions are employed on the streamwise direction. Periodic boundary conditions are used at the side, top, and bottom boundaries of the domain. In Appendix B we show the results of our domain validation study, demonstrating that the sizes of the computation domain used in our DNS are sufficiently large and that the use of periodic boundary conditions does not affect the results.

The conformation tensor equation is solved with the method of Vaithianathan *et al.* [51], which is based on the shock-capturing scheme of Kurganov and Tadmor [52], for the advection term, and makes no use of any artificial numerical diffusion. It was verified that this method provided second-order accuracy at more than 98% of the points of the domain. The values of the conformation tensor were monitored throughout the simulations and it was verified that the symmetric and positivedefinite properties were preserved. Second-order central finite differences are used for the stretching term of the conformation tensor equation.

The scalar equation uses pseudospectral and sixth-order compact schemes, for the evaluation of the diffusion term, and a second-order QUICK scheme for the advection term [44,53]. In a typical simulation, small undershoot ($\theta < 0$) and overshoot ($\theta > 1$) values are found at about 2% of the computational points, similarly to previous DNS studies [5] employing the QUICK scheme.

C. Physical and computational parameters

For jets and wakes, the inlet velocity field is prescribed as the sum of mean and fluctuating components. The inlet mean components of the planar jet are given by

$$\bar{u} = \frac{U_J + U_\infty}{2} + \frac{U_J - U_\infty}{2} \tanh\left[\frac{h}{4\Phi}\left(1 - \frac{2|y|}{h}\right)\right], \tag{6}$$

$\bar{v} = \bar{w} = 0$, where U_J and U_∞ are the jet centerline velocity at the inlet and a small coflow velocity at the inlet, respectively. The prescribed values are $U_J = 1.091$ and $U_\infty = 0.091$ (arbitrary units for the velocities). The inlet mean velocity components of the planar wake are

$$\bar{u} = U_\infty - \frac{\Delta U_0}{2}\left\{1 + \tanh\left[\frac{d}{4\Phi}\left(1 - \frac{2|y|}{d}\right)\right]\right\}, \tag{7}$$

and $\bar{v} = \bar{w} = 0$, where the free stream velocity is U_∞ and the inlet centerline velocity deficit is ΔU_0. The adopted values are $U_\infty = 1$ and $\Delta U_0 = 0.2$ (arbitrary units). h and d are the slot width of the jet and the transverse length scale of the wake object, respectively. The parameter h/Φ quantifies the strength of the gradients at the inlet; for jets, it is the inverse of the normalized momentum thickness. The values used here are $h/\Phi = 30$, for jets, and $d/\Phi = 60$, for wakes.

The fluctuating components of the inlet velocity profile are obtained from a pseudorandom number generator, and have energy spectra characteristic of isotropic turbulence, that are imposed predominantly at the shear-layer region of the inlet mean velocity profile [9,14,54]. The values of the maximum amplitudes of the inlet noise, normalized by U_J for jets and U_∞ for wakes, are equal to 0.15 for jets and 0.1 for wakes, respectively.

The scalar field at the inlet $x = 0$ is prescribed using the following formula:

$$\theta = \frac{\theta_c^{\rm in} + \theta_\infty^{\rm in}}{2} + \frac{\theta_c^{\rm in} - \theta_\infty^{\rm in}}{2} \tanh\left[\frac{h}{4\Phi}\left(1 - \frac{2|y|}{h}\right)\right], \tag{8}$$

where $\theta_c^{\rm in}$ is the centerline ($y = 0$) value of θ and $\theta_\infty^{\rm in}$ is the free stream value of θ at the inlet. For wakes, the transverse length scale d of the wake generator object appears in place of the width of the jet slot h. Numerically, we set $\theta_c^{\rm in} = 1$ and $\theta_\infty^{\rm in} = 0$ for both jets and wakes. The obtained profile is typical of a heated jet issuing into a cold environment or of a cold stream flowing through a hot wake object.

The hyperbolic tangent profile of Eqs. (6)–(8) provides an excellent fit to the inlet mean profiles that are measured in experiments [55–57]. Additionally, it has been used as the base flow of linear stability calculations that are able to predict very accurately the evolution of shear-layer perturbations [58–60]; the same for direct numerical simulations of transitioning and fully turbulent flows [8,9,14,44,46,61–64].

The conformation tensor components at the inlet are prescribed with the analytical solutions of the laminar Couette flow for the FENE-P fluid, using the values of the local mean velocity gradient at each grid point [43,65]. This is the solution that is consistent with the velocity field [14,43,65], and it was also used in linear stability calculations of viscoelastic jets [13] whose results were confirmed later in experiments [11] and DNSs [14].

A total of four Newtonian and nine viscoelastic DNSs of turbulent jets and wakes were carried out in the present work, and Table I summarizes the main physical and computational parameters used for these simulations. The results of 21 additional simulations, which were conducted to test Reynolds number effects, mesh resolution, and the sizes of the computational domain, are discussed in the Appendixes. For jets the inlet Reynolds number is defined as $\text{Re} = (U_J - U_\infty)h/\nu^{[s]}$ and the inlet Weissenberg number is defined as $\text{Wi} = \tau_p(U_J - U_\infty)/h$, whereas for wakes they are $\text{Re} = \Delta U_0 d/\nu^{[s]}$ and $\text{Wi} = \tau_p \Delta U_0/d$, respectively. The domain sizes in each spatial direction are $L_{\rm x}$, $L_{\rm y}$, and $L_{\rm z}$ and the number of grid points in each direction of the uniform mesh are $n_{\rm x}$, $n_{\rm y}$, and $n_{\rm z}$. The Schmidt number based on the diffusivity coefficient of the passive scalar $\text{Sc} = \nu^{[s]}/D$ is set to $\text{Sc} = 1$ for all DNS.

The Taylor microscale $\lambda = (15\nu^{[s]}\overline{u'^2}/\varepsilon^{[s]})^{1/2}$, root-mean-squared (rms) velocity $\sqrt{\overline{u'^2}}$, and solvent mean viscous dissipation rate of the turbulent kinetic energy $\varepsilon^{[s]} = 2\nu^{[s]}\overline{S'_{ij}S'_{ij}}$ are used in the definition of the local Taylor Reynolds number $\text{Re}_\lambda = \sqrt{\overline{u'^2}}\lambda/\nu^{[s]}$, where $S'_{ij} = (\partial u'_i/\partial x_j + \partial u'_j/\partial x_i)/2$ is the fluctuating component of the rate-of-strain tensor. The resolution of the DNS is quantified by calculating the Kolmogorov length scale $\eta = (\nu^{[s]^3}/\varepsilon^{[s]})^{1/4}$ and the grid spacing Δx.

For local quantities, Table I shows values that are characteristic of the far field, at $x = 0.8L_{\rm x}$. The largest values of the grid resolution parameter $\Delta x/\eta$ in the whole domain, $(\Delta x/\eta)_{\rm max}$, are also listed in Table I. This ratio quantifies the resolution at the position where the grid is the coarsest relative to the Kolmogorov length scale. This is typically attained at the end of the transition region, and starts to decay along the flow direction, so that the relative resolution of the uniform grid is always better at the fully turbulent far field, which is the region of interest in this work.

TABLE I. Physical and computational parameters of the simulations: inlet Weissenberg number [$\mathrm{Wi} = \tau_p(U_J - U_\infty)/h$, for jets, and $\mathrm{Wi} = \tau_p \Delta U_0/d$, for wakes]; inlet Reynolds number [$\mathrm{Re} = (U_J - U_\infty)h/\nu^{[s]}$, for jets, and $\mathrm{Re} = \Delta U_0 d/\nu^{[s]}$, for wakes]; reference polymer concentration parameter [$1-\beta = 1 - \nu^{[s]}/(\nu^{[s]} + \nu^{[p]})$]; maximum length of the polymer dumbbells normalized by their equilibrium radius (L); Taylor-based Reynolds number at the far-field shear-layer region (Re_λ at $x = 0.8L_\mathrm{x}$ and $y/\delta = 1$); grid spacing normalized by the Kolmogorov microscale ($\Delta x/\eta$), at the position where $\Delta x/\eta$ attains its largest value, and also at the far-field region at $x = 0.8L_\mathrm{x}$ (centerline); dimensions of the computational domain in each direction (L_x, L_y, and L_z) normalized by h, for jets, and by d, for wakes; number of points of the computational grid in each spatial direction (n_x, n_y, and n_z). NA stands for not applicable.

Flow type	Wi	Re	$1-\beta$	L	Re_λ	$(\frac{\Delta x}{\eta})_{\max}$	$(\frac{\Delta x}{\eta})_{0.8L_\mathrm{x}}$	$\frac{L_\mathrm{x}}{h} \times \frac{L_\mathrm{y}}{h} \times \frac{L_\mathrm{z}}{h}$	$n_\mathrm{x} \times n_\mathrm{y} \times n_\mathrm{z}$
	0	3500	NA	NA	114	2.5	2.0	$20 \times 20 \times 4.5$	$1024 \times 1024 \times 256$
	3	3500	0.20	100	290	1.8	1.7	$20 \times 20 \times 4.5$	$768 \times 768 \times 174$
	3	3500	0.02	100	208	3.0	2.4	$20 \times 20 \times 4.5$	$576 \times 576 \times 128$
Jet	3	3500	0.10	100	300	2.5	2.4	$20 \times 20 \times 4.5$	$576 \times 576 \times 128$
	3	3500	0.20	100	311	2.4	2.3	$20 \times 20 \times 4.5$	$576 \times 576 \times 128$
	0	2500	NA	NA	211	2.8	1.2	$52.8 \times 44.44 \times 4.44$	$1824 \times 1536 \times 154$
	0	2500	NA	NA	211	4.4	1.3	$97.8 \times 80 \times 4.45$	$2112 \times 1728 \times 96$
	5	2500	0.04	200	206	2.4	1.3	$97.8 \times 80 \times 4.45$	$2112 \times 1728 \times 96$
	5	2500	0.02	200	260	3.7	1.9	$97.8 \times 80 \times 4.45$	$1408 \times 1152 \times 64$
	0	2000	NA	NA	65	2.5	1.3	$198 \times 16.5 \times 4.55$	$6912 \times 576 \times 160$
Wake	5	2000	0.10	200	98	1.7	0.8	$198 \times 16.5 \times 4.55$	$6912 \times 576 \times 160$
	3	2000	0.02	200	107	1.6	1.1	$198 \times 16.5 \times 4.55$	$6912 \times 576 \times 160$
	5	2000	0.02	100	102	1.9	0.9	$198 \times 16.5 \times 4.55$	$6912 \times 576 \times 160$

Our mesh resolution study in Appendix A demonstrates that our simulations are well resolved. Appendix B shows that the sizes of the computational domains are large enough to allow the natural evolution of the flows. For maximum clarity only the statistics of the DNS at the largest computational domains will be shown in the main body of this paper. Statistics of other simulations are shown in Appendix E, where we also include some complementary data that was omitted from the main body, to enhance its readability, and in Appendix C, where we discuss Reynolds number effects on the statistics. Comparison between the new DNS data and experimental data from the literature are presented in Appendix D.

For turbulent planar jets we define the shear-layer half-width $\delta(x)$ as in Guimarães *et al.* [8], i.e., based on an integral of the normalized mean velocity profile, whereas for wakes we adopt the classical definition given by $\Delta\bar{u}(x, y = \delta) = \Delta U(x)/2$, where $\Delta\bar{u}(x, y) = U_\infty - \bar{u}(x, y)$ is the mean velocity deficit and $\Delta U(x) = \Delta\bar{u}(x, y = 0)$ is the local velocity deficit at the centerline. The scaling laws for the jet centerline mean velocity $U_c(x)$ and $\delta(x)$ are given by

$$\left[\frac{U_c(x)}{U_J}\right]^{-2} = A_{U_c}\left(\frac{x - x_0}{h}\right), \quad \frac{\delta(x)}{h} = A_\delta\left(\frac{x - x_0}{h}\right), \tag{9a,b}$$

where x_0 is the virtual origin and A_δ and A_{U_c} are the jet spreading and decay rates, respectively. The scaling laws for the wake centerline mean velocity deficit and $\delta(x)$ are given by

$$\left[\frac{\Delta U(x)}{U_\infty}\right]^{-2} = A_{\Delta U}\left(\frac{x - x_0}{d}\right), \quad \left[\frac{\delta(x)}{d}\right]^2 = A_{\delta^2}\left(\frac{x - x_0}{d}\right), \tag{10a,b}$$

where A_{δ^2} and $A_{\Delta U}$ are the wake spreading and decay rates, respectively.

Guimarães *et al.* [8,9] performed a similarity analysis of the equations that govern the mean flow and showed that the scaling laws of Eqs. (9a,b) and (10a,b) are also valid for viscoelastic fluids. The result is independent of the rheological model (see Guimarães *et al.* [8,9]), but different scaling law coefficients are obtained at the high and low elasticity regions of the far-field, corresponding to high and low local Deborah numbers $\mathrm{De}(x)$, where $\mathrm{De}(x) = \tau_p U_c/\delta$ for jets and $\tau_p \Delta U/\delta$ for wakes, respectively.

The shear-layer width based on the mean scalar $[\delta_\theta(x)]$ is defined by $\overline{\theta}(x, y = \delta_\theta) = \theta_c(x)/2$, where $\theta_c(x) = \overline{\theta}(x, y = 0)$. For Newtonian planar jets the scaling laws for the passive scalar are given by [66]

$$\left[\frac{\theta_c(x)}{\theta_0}\right]^{-2} = A_{\theta_c}\left(\frac{x - x_0}{h}\right), \quad \frac{\delta_\theta(x)}{h} = A_{\delta_\theta}\left(\frac{x - x_0}{h}\right), \tag{11a,b}$$

where $\theta_0 = \theta_c(x = 0)$. For Newtonian planar wakes, the passive scalar scaling laws are [66]

$$\left[\frac{\theta_c(x)}{\theta_0}\right]^{-2} = A_{\theta_c}\left(\frac{x - x_0}{d}\right), \quad \left[\frac{\delta_\theta(x)}{d}\right]^{2} = A_{\delta_\theta^2}\left(\frac{x - x_0}{d}\right). \tag{12a,b}$$

Our DNS results indicate that the above passive scalar scaling laws are not valid for viscoelastic fluids at the high elasticity region of the far field, because there the mean scalar profiles are not self-similar. Only at the low elasticity region of the far-field are the scaling laws for the passive scalar valid.

III. THE EVOLUTION AND MIXING OF PASSIVE SCALARS

A. Classical statistics

The downstream development of the normalized scalar half-width $[\delta_\theta(x)]$ and mean centerline scalar $[\theta_c(x)]$ are displayed in Fig. 1 while the normalized scalar variances are shown in Fig. 2, for jets and wakes. The behavior of these quantities resembles that documented for the flow half-width, centerline mean, and rms velocities [8,9], described below, but shows also some differences. In particular, the scalar field seems to be much more sensitive to viscoelasticity—this larger sensitivity was also observed for wall flows [4].

For the Newtonian jet, the mean scalar width starts to grow and its magnitude starts to decay according to a self-similar development at $x/h \approx 5$ [Figs. 1(a) and 1(b)], with a scalar spreading rate of $A_{\delta_\theta} = 0.13$, and scalar decay rate of $A_{\theta_c} = 0.32$, using the best-fit values between $20 \leqslant x/h \leqslant 90$, for A_{δ_θ}, and $20 \leqslant x/h \leqslant 40$, for A_{θ_c} (A_{δ_θ} was obtained from the DNS at a smaller domain and higher resolution; see Table I and Appendix A). The viscoelastic jet with $\mathrm{Wi} = 5$, $L = 200$, and $1 - \beta = 0.02$ shows a region of quasizero scalar growth and decay that extends up to $x/h \approx 10$, followed by an intermediate region where the scalar spread is very intense, with $A_{\delta_\theta} = 0.161$ at $20 < x/h < 90$, corresponding to a 24% increase of A_{δ_θ} in comparison to the Newtonian value, and the decay rate of mean scalar is $A_{\theta_c} = 0.438$, i.e., a 27% increase of A_{θ_c}. The jet at the higher polymer concentration ($1 - \beta = 0.04$) displays a similar behavior, but the initial region of quasizero scalar growth and decay is slightly larger.

The scalar field of the Newtonian planar wake starts to grow in width, and its magnitude starts to decay, at $x/d \approx 20$ [Figs. 1(c) and 1(d)] with $A_{\delta_\theta^2} = 0.023$ and $A_{\theta_c} = 0.128$, using the best-fit values between $60 \leqslant x/d \leqslant 180$. The viscoelastic wake of the very dilute polymer solution with $\mathrm{Wi} = 3$, $1 - \beta = 0.02$, and $L = 200$, shows a region of quasizero scalar growth and decay that extends up to $x/d \approx 60$, while for the wake with the most intense viscoelastic effects, i.e., the semidilute case with $\mathrm{Wi} = 5$, $1 - \beta = 0.10$, and $L = 200$, this initial region extends up to $x/d \approx 140$. Considering the case with a very dilute polymer solution and the smallest molecular weight, with $\mathrm{Wi} = 5$, $1 - \beta = 0.02$, and $L = 100$, the scalar field starts to grow and decay at the same position of the Newtonian wake, at $x/d \approx 20$, and the values of $A_{\delta_\theta^2}$ and A_{θ_c} are not very different from the Newtonian values.

The wake with $\mathrm{Wi} = 3$, $1 - \beta = 0.02$, and $L = 200$, contains a second region with an intensified scalar spreading rate at $x/d \gtrsim 120$, similarly to the jet flow cases. For that case we obtain $A_{\delta_\theta^2} = 0.040$ and $A_{\theta_c} = 0.245$ at $120 < x/d < 180$, corresponding to a strong increase of the scalar spreading and decay rates, in comparison to the Newtonian case, by factors of nearly 2. We expect

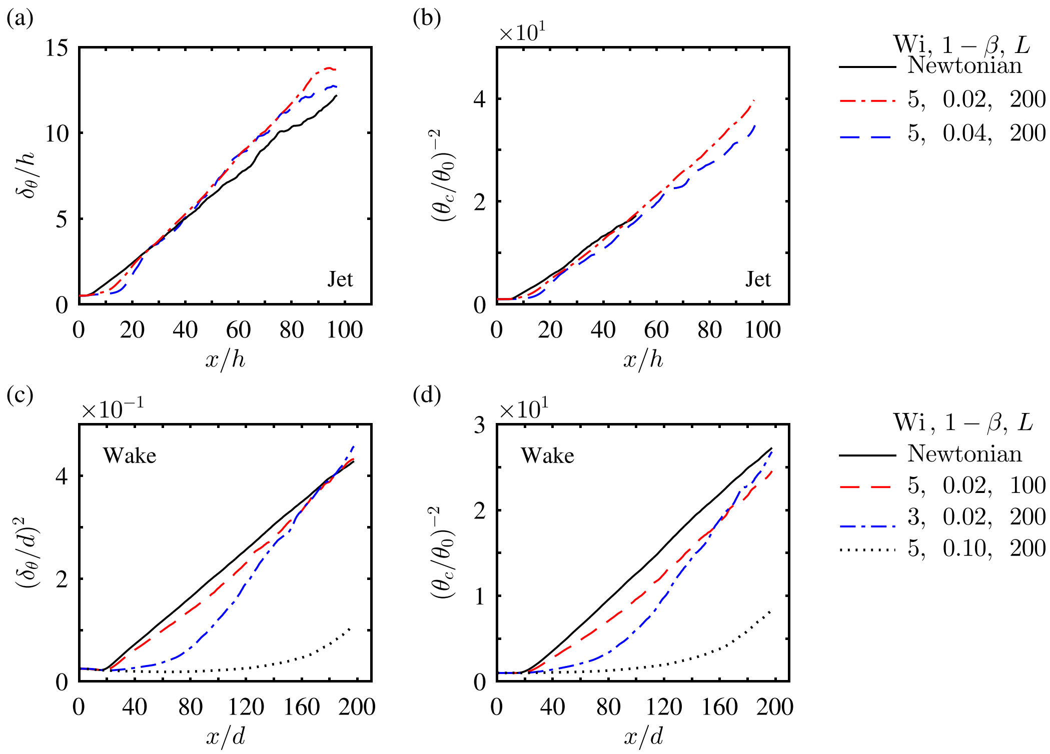

FIG. 1. Streamwise evolution of the normalized scalar half-width (a),(c), and centerline mean scalar (b),(d), for jets (a),(b), and wakes (c),(d). The Newtonian curve in panel (b) was obtained from the DNS at a relatively smaller domain and higher resolution (see Table I and Appendix A).

a similar trend for the wake with Wi $= 5$, $1-\beta = 0.10$, and $L = 200$, but only at much farther distances, at $x/d \gg 200$ (well beyond our computational domain), since for this case the initial region with a quasizero scalar spreading and decay is also much longer.

Considering now the normalized scalar variance, shown in Fig. 2, the effect of viscoelasticity for large Wi flows with $L = 200$ is to initially decrease the values of $\sqrt{\overline{\theta'^2}}/\theta_c$, but that is followed by a region where $\sqrt{\overline{\theta'^2}}/\theta_c$ is enhanced by viscoelasticity, with jets and wakes also exhibiting some quantitative differences. For the jet flow with the highest polymer concentration, the region of scalar variance suppression is $4 \lesssim x/h \lesssim 13.3$: at $x/h = 9$, where the peak value is located for the Newtonian jet, the normalized scalar variance is reduced by a factor of 3. In contrast, at $x/h = 25$ the normalized scalar variance for the viscoelastic jet can be three times higher than the value obtained for the Newtonian jet. Farther downstream $\sqrt{\overline{\theta'^2}}/\theta_c$ decays towards a plateau whose value is much closer to the Newtonian plateau value, but that is still slightly higher for the viscoelastic cases. Similar trends can be observed for the wake flows with $L = 200$ [Fig. 2(b)]. The very dilute wake with $L = 100$ is different from other cases as it does not show an initial region with a scalar variance suppression—only scalar variance enhancement is observed at the far field, suggesting that in this case viscoelasticity is not strong enough to suppress the scalar fluctuations in the near field.

The spread and decay of the scalar field described above is the result of the large-scale stirring and small-scale mixing of the scalar promoted by the turbulent flow [67,68], which will be analyzed in the next sections in order to explain the observed results. We will show that the large reduction of the spreading and decay rates of passive scalars at the near field is caused by a suppression of the small-scale mixing and large-scale stirring promoted by the polymers in that region, whereas

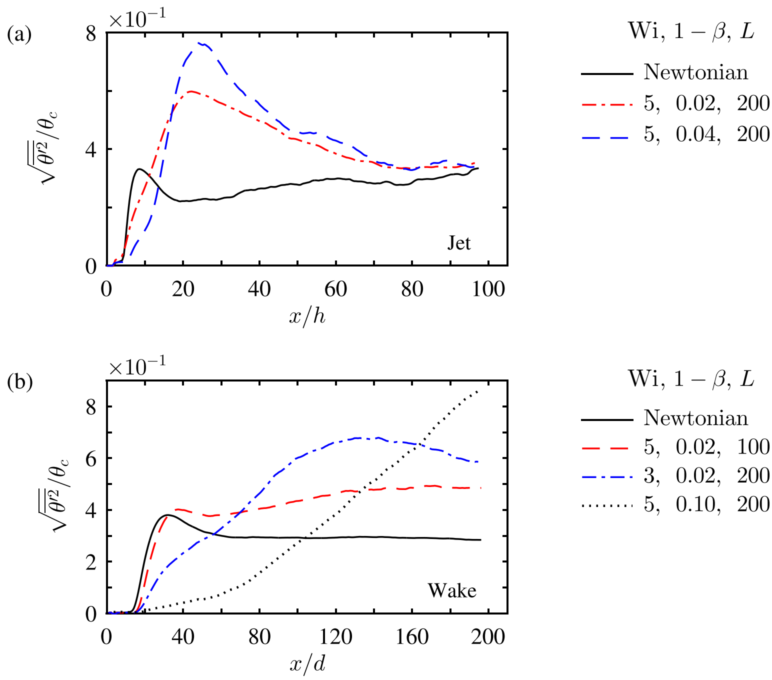

FIG. 2. Streamwise evolution of the normalized scalar variance at the centerline for jets (a) and wakes (b).

at the very far field the suppression of the small-scale mixing is compensated by an increase of the large-scale stirring, resulting in larger spreading and decay rates.

B. Small-scale mixing

For statistically stationary fully developed turbulent flows, a useful quantity for characterizing the degree of small-scale scalar mixing is the normalized dissipation of half scalar variance [68,69]: $\varepsilon_\theta/(\sqrt{\kappa_c}\overline{\theta'^2}_c/\delta)$, where $\varepsilon_\theta = D\overline{(\partial\theta'/\partial x_i')^2}$, $\kappa = (\overline{u'^2} + \overline{v'^2} + \overline{w'^2})/2$ is the turbulent kinetic energy, and the subscript c indicates quantities evaluated at the flow centerline.

Transverse profiles of normalized dissipation of scalar variance, at two different x stations of jets and wakes, are shown in Fig. 3. The influence of viscoelasticity is to decrease the values of $\varepsilon_\theta/(\sqrt{\kappa_c}\overline{\theta'^2}_c/\delta)$ and thus to decrease the level of mixing; reductions by a factor larger than 4 are observed for some cases. In contrast, one case shows also an initial increase of the scalar dissipation, the wake flow with the largest viscoelasticity, with $1 - \beta = 0.10$ and $L = 200$, but only for a small portion of the profile at $x/d = 70$ and $0.2 \lesssim y/\delta \lesssim 0.7$, possibly due to its longer transition region so that at $x/d = 70$ the turbulence is not yet fully developed for that case. At $x/d = 160$, this case also shows a drastic decrease of scalar dissipation for all y locations.

The large mixing rates that are characteristic of turbulent flows are a result of the highly contorted and thus enlarged isoscalar surface areas that are generated by turbulence at the small scales [67,70]. Guimarães *et al.* [8,9] observed that viscoelasticity leads to a suppression of small-scale turbulence, and the isovorticity contours look “smoother” and less contorted for viscoelastic jets and wakes, in comparison to Newtonian flows. Fractal dimension calculations of a turbulent interface confirmed that viscoelasticity results in a smaller fractal dimension and surface area of the interface when viscoelasticity is high (see Table 3 of Abreu *et al.* [18]). Hence, it is natural to expect that the reduced levels of scalar mixing observed here for highly viscoelastic flows should be a consequence of the smaller isoscalar surface areas that result from the suppression of small-scale turbulence caused

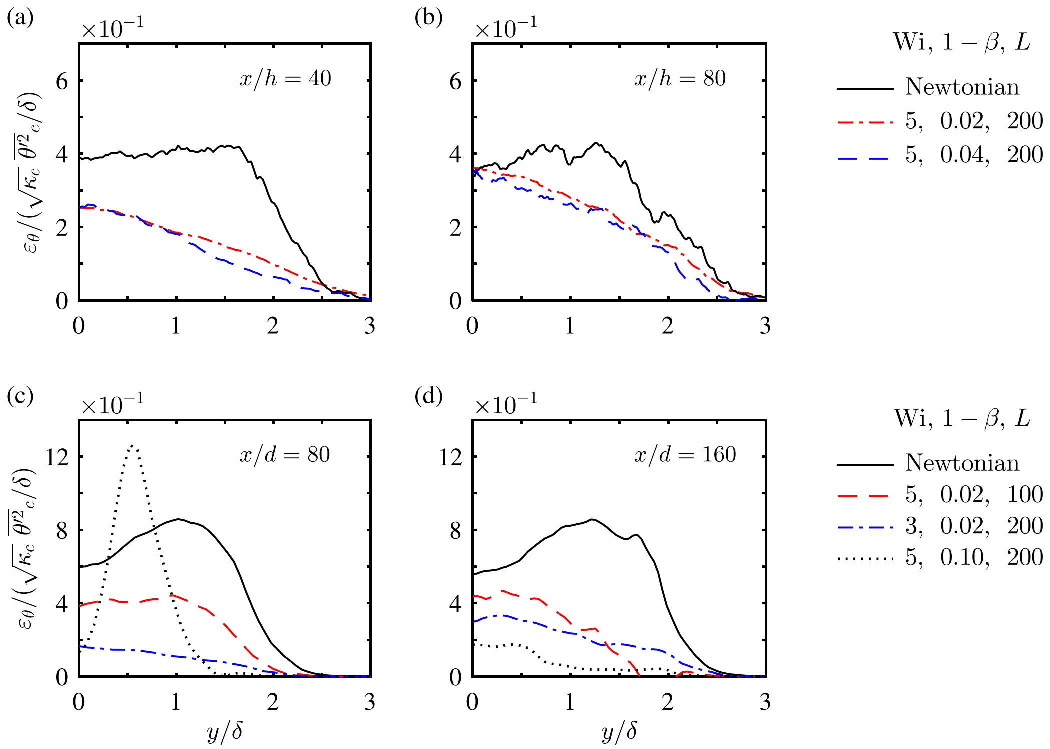

FIG. 3. Transverse y profiles of the normalized dissipation of scalar variance for jets (a),(b) and wakes (c),(d) at different x stations.

by the polymers. Two-dimensional contours of the instantaneous scalar field shown in Figs. 4–6 suggest that this is indeed the case.

The reduced rate of passive scalar mixing for highly viscoelastic cases discussed above is also evident from Figs. 4–6, as near unity θ values corresponding to unmixed hot fluid can still be seen even at dozens of diameters downstream from the inlet, at locations where the scalar of the Newtonian case has already mixed considerably. This is corroborated in Fig. 7, which shows

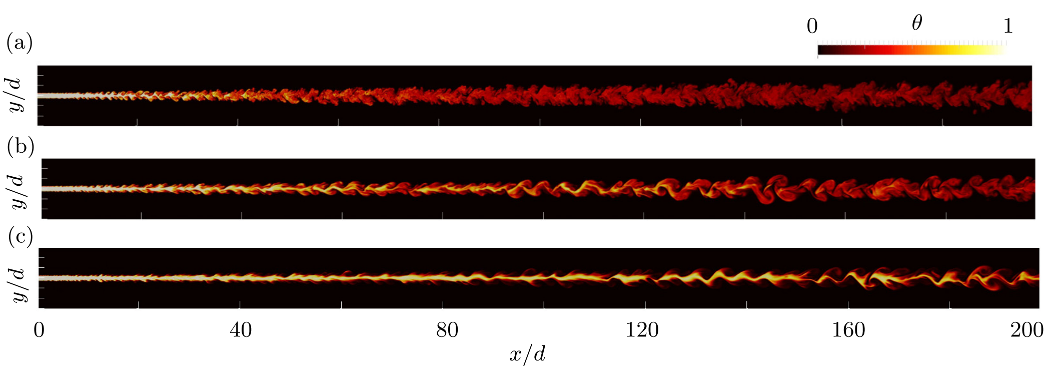

FIG. 4. Two-dimensional contours of the instantaneous passive scalar field for (a) Newtonian wake at Re = 2000; (b) viscoelastic wake at Re = 2000, Wi = 3, $1-\beta = 0.02$, and $L = 200$; and (c) viscoelastic wake at Re = 2000, Wi = 5, $1-\beta = 0.10$, and $L = 200$.

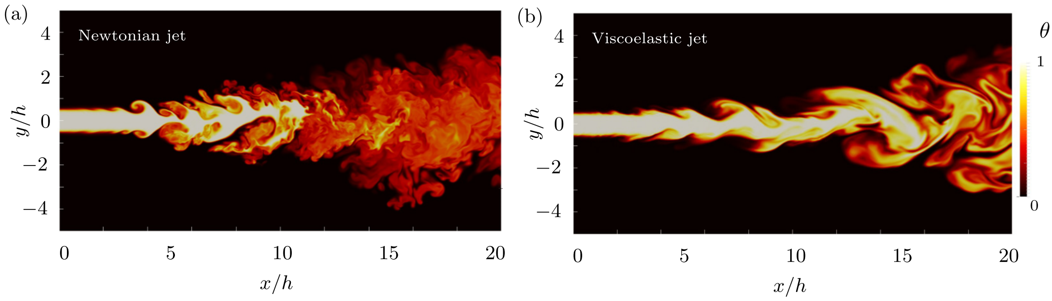

FIG. 5. Two-dimensional contours of the instantaneous passive scalar field for (a) Newtonian jet at Re = 3500 and (b) viscoelastic jet at Re = 3500, Wi = 3, $1-\beta = 0.20$, and $L = 100$.

probability density functions of θ at $x/d = 100$ and four different y/δ_θ locations for Newtonian and viscoelastic wakes. The geometric shape of the curves for Newtonian and viscoelastic flows is of course very different, but the most striking feature is that even for this very far x distance there is still a nonzero probability of finding nearly unmixed fluid with θ close to unity, for the viscoelastic flows, whereas for the Newtonian flow the scalar is already well mixed and the probability of finding $\theta > 0.5$ is negligibly small. Similar results were observed for jets (Appendix E).

C. Large-scale stirring

The normalized lateral fluxes of mean scalar and scalar variance, $\overline{v'\theta'}/(U_c\theta_c)$ and $\overline{v'\theta'^2}/(U_c\theta_c^2)$ (ΔU is used for wakes), respectively, can be used for quantifying the levels of large and intermediate scale stirring [71]. DNS results of channel flow with viscoelastic fluids [3] have shown a strong increase of the streamwise scalar flux, i.e., the horizontal component $\overline{u'\theta'}$ (properly normalized) caused by viscoelasticity, and a decrease of the lateral component, and therefore the horizontal component may also contribute to stirring for the viscoelastic flows and will also be analyzed here.

The streamwise evolutions of the normalized turbulent fluxes of mean scalar are shown in Figs. 8(a)–8(d), for jets and wakes, respectively. In general terms, the influence of viscoelasticity on these fluxes is similar to that described for the mean scalar half-width and centerline mean scalar and scalar variance and indeed can be used to explain the evolution of these quantities; an initial depletion of the turbulent flux (less stirring) is followed by a strong enhancement (more stirring) and finally a reduction to values that are closer to the Newtonian values at the very far regions, but that remain higher for some cases. This becomes more pronounced as viscoelasticity is increased.

The streamwise ($\overline{u'\theta'}$) and transverse ($\overline{v'\theta'}$) turbulent fluxes follow similar trends in terms of the downstream evolution, but there are also some important differences between these two components. The extent of the initial x region with a turbulent flux depletion caused by viscoelasticity is longer for $\overline{v'\theta'}$ than for $\overline{u'\theta'}$. This results in an intermediate flow region ($10 \lesssim x/h \lesssim 15$ for jets and $50 \lesssim x/d \lesssim 100$ for wakes) where viscoelasticity enhances the normalized $\overline{u'\theta'}$ component but decreases the $\overline{v'\theta'}$ component, similarly to the behavior observed for channel flow [3]. Additionally, where the normalized $\overline{u'\theta'}$ component is intensified by viscoelasticity the increase can be very strong—up to six times the Newtonian values for the more pronounced case—while where the normalized $\overline{v'\theta'}$ component is intensified by viscoelasticity the increase is milder—not even twice the value of the Newtonian flow. The normalized turbulent flux of scalar variance $\overline{v'\theta'^2}/(U_c\theta_c^2)$ was also analyzed and revealed a similar behavior (Appendix E).

The physical mechanism responsible for the increased levels of large-scale stirring at the far field can be elucidated by the analysis of the turbulent structures of the flow. Two-dimensional contours of instantaneous velocity fluctuation $u' = u - \bar{u}$ are shown in Fig. 9 for Newtonian and viscoelastic jets at Re = 3500. Considering the region at $x/h \gtrsim 12$, where the scalar variance flux is considerably enhanced by viscoelasticity, the turbulent structures of the Newtonian jet are much more fragmented

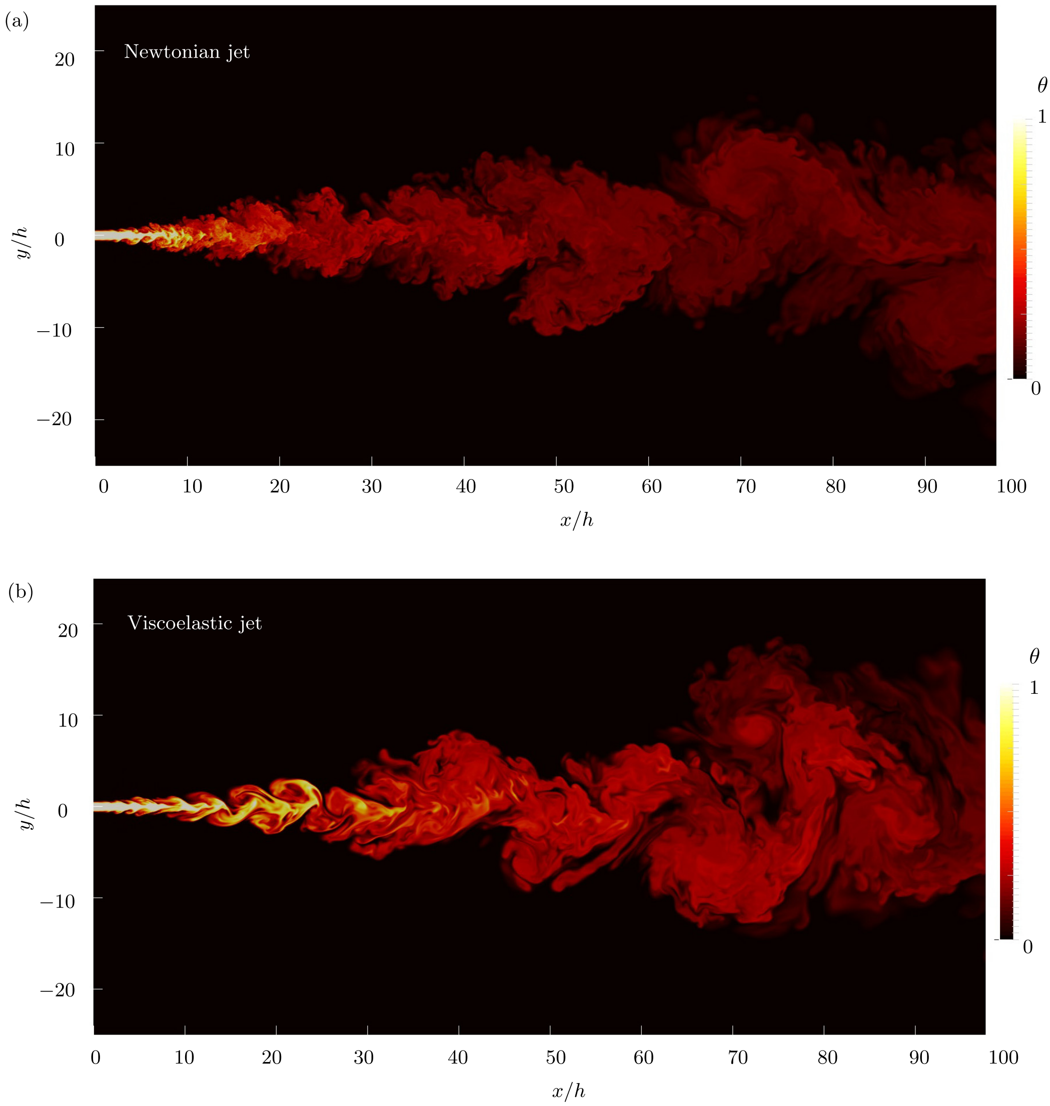

FIG. 6. Two-dimensional contours of the instantaneous passive scalar field for (a) Newtonian jet at Re = 2500 and (b) viscoelastic jet at Re = 2500, Wi = 5, $1 - \beta = 0.02$, and $L = 200$.

in comparison to those of the viscoelastic jet. The viscoelastic jet exhibits longer and more coherent structures on the streamwise direction, a condition that promotes the flux of passive scalar on that direction [3].

The analysis of the contours of transverse velocity fluctuations $v' = v - \bar{v}$, shown in Fig. 10, leads to similar conclusions, but the structures of v' of the viscoelastic jet exhibit larger coherence on the transverse direction, instead of the streamwise direction. The corresponding structures of fluctuating passive scalar $\theta' = \theta - \bar{\theta}$, displayed in Fig. 11, lead again to similar conclusions.

The fragmentation of the large-scale structures is initiated by three-dimensional perturbations at the small scales. Since the small-scale turbulent fluctuations are attenuated by the polymers, the large-scale structures of viscoelastic flows are able to survive (i.e., keep their coherence) over longer

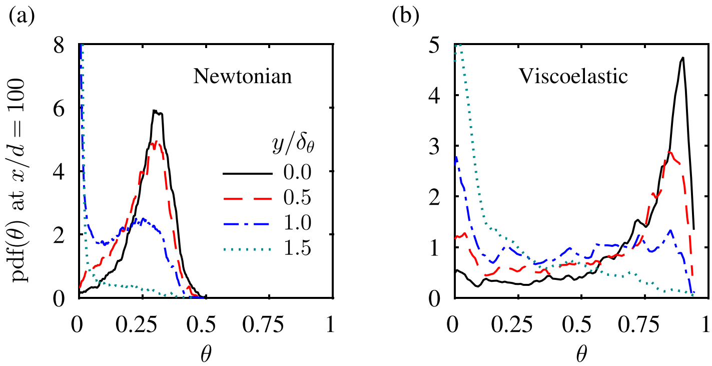

FIG. 7. Scalar probability density function distribution at four y/δ_θ positions at $x/d = 100$ for (a) Newtonian wake and (b) viscoelastic wake with Wi = 5, $1 - \beta = 0.10$, and $L = 200$. Notice the different scales used for the ordinates of the graphs in each figure. Jet results show similar trends (Appendix E).

periods of time and distances in comparison to Newtonian flows, which explains the results reported in the paragraphs above.

The turbulent structures of the jet simulations at a larger domain size and Re = 2500 show a similar behavior up to $x/h \approx 60$ (Fig. 12). Downstream from that region, at $x/h \gtrsim 60$, the structures of Newtonian and viscoelastic flows are not very different, which explains the similar statistics. In fact, the region where we observe most differences in turbulent structures is around $x/h \approx 25$, and

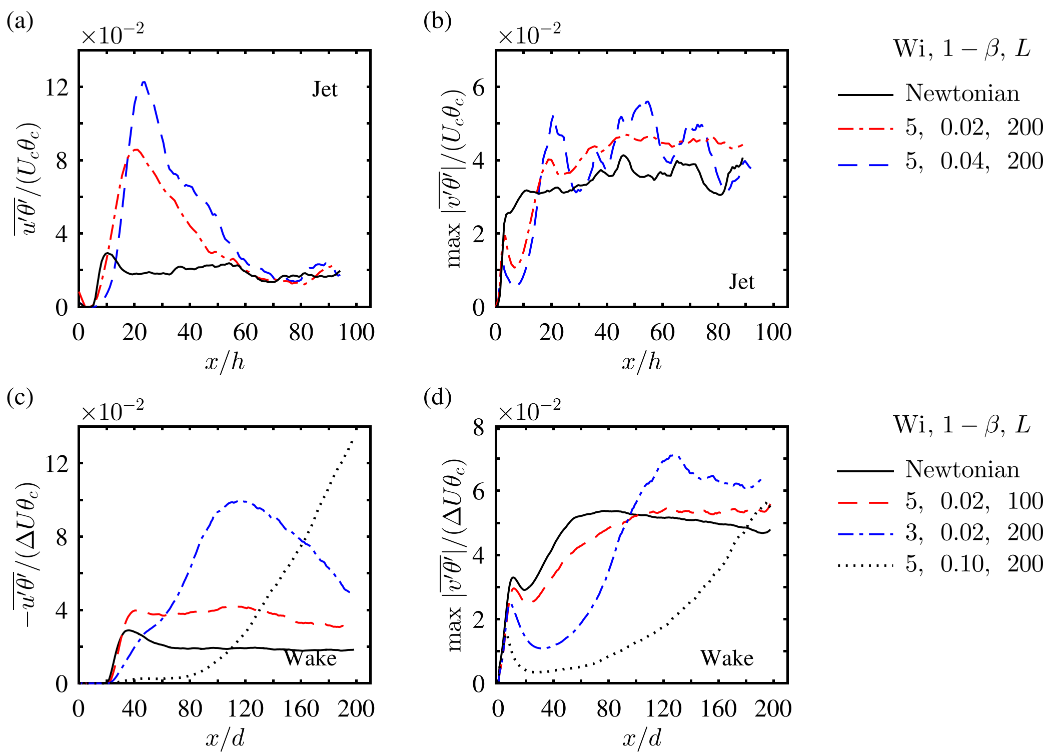

FIG. 8. Streamwise evolution of the normalized turbulent fluxes of mean scalar for jets (a),(b) and wakes (c),(d). The horizontal flux is evaluated at the flow centerline, while the maximum values are shown for the lateral flux.

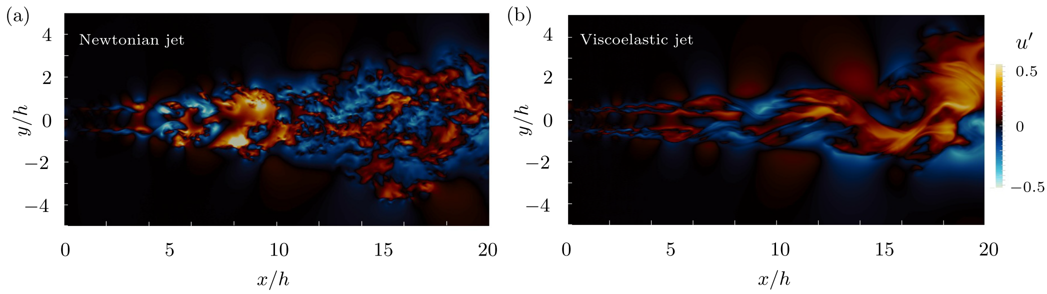

FIG. 9. Two-dimensional contours of instantaneous streamwise velocity fluctuation $u' = u - \bar{u}$ at $z = 0$: (a) Newtonian jet at Re = 3500 and (b) viscoelastic jet at Re = 3500, Wi = 3, $1 - \beta = 0.2$, and $L = 100$.

corresponds to the region where the turbulent statistics, such as the scalar variance and turbulent scalar fluxes, are affected the most by viscoelasticity. This corroborates the argument that the enhancement of the large-scale stirring at the far field is a result of the polymer action on the turbulent structures. The decrease of viscoelastic effects at the very far regions can be explained by the decaying character of the local Deborah and Weissenberg numbers, as reported in previous works [8,9]. The turbulent structures pertaining to the turbulent planar wake simulations revealed a similar qualitative behavior (Fig. 13).

The suppression of the large-scale stirring of passive scalars at the near field might be explained by the stabilization of flow perturbations caused by the polymers at the nonlinear region of the transition to turbulence [14,72]. The nonlinear stabilization mechanism was investigated and explained in detail in Guimarães *et al.* [14]. Since the passive scalar field is more sensitive to the viscoelasticity than the velocity field [1], it is possible that this stabilization mechanism is prolonged further downstream for the fluctuating passive scalar, than for the velocity fluctuations. The linear destabilization mechanism of viscoelasticity [13,14] is not relevant for the flows considered in this paper because of the relatively large velocity fluctuations imposed at the inlet ($u'/\bar{u} \sim 0.10$ at $x = 0$) that precludes the existence of a linear region of perturbation growth.

D. Reynolds analogy

Of particular importance in engineering applications is the concept of turbulent (eddy) diffusivities of momentum and scalar, given by $\nu_t = -\overline{u'v'}/(\partial\bar{u}/\partial y)$ and $\alpha_t = -\overline{v'\theta'}/(\partial\bar{\theta}/\partial y)$, respectively, and the turbulent Schmidt number $\mathrm{Sc}_t = \nu_t/\alpha_t$ (known as the Prandtl number when the scalar is the temperature field). These formulas allow the implementation of simple mean flow calculations and provide measures for the efficiency of large-scale turbulent diffusion of momentum and scalars. A constant, near unity Sc_t results from the Reynolds analogy between momentum and scalar transfer.

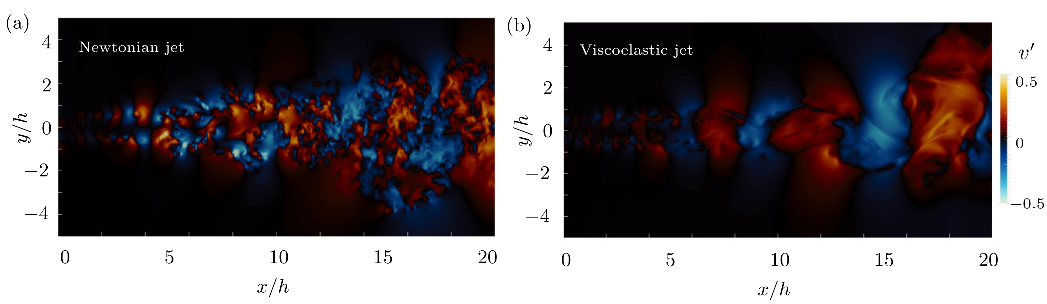

FIG. 10. Two-dimensional contours of the instantaneous transverse velocity fluctuation $v' = v - \bar{v}$ at $z = 0$: (a) Newtonian jet at Re = 3500 and (b) viscoelastic jet at Re = 3500, Wi = 3, $1 - \beta = 0.2$, and $L = 100$.

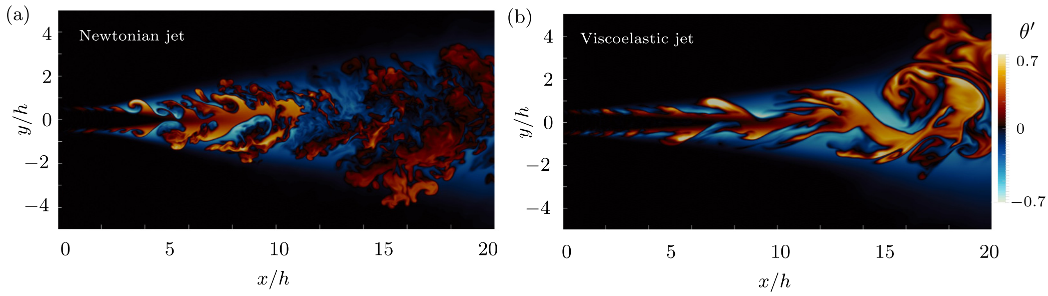

FIG. 11. Two-dimensional contours of the instantaneous passive scalar fluctuation $\theta' = \theta - \bar{\theta}$ at $z = 0$: (a) Newtonian jet at Re = 3500 and (b) viscoelastic jet at Re = 3500, Wi = 3, $1 - \beta = 0.2$, and $L = 100$.

For Newtonian jets and wakes a self-similar evolution of both ν_t and α_t is obtained when these are scaled by $U_c\delta$ or $\Delta U\delta$, for jets and wakes, respectively. The normalized transverse profiles of both diffusivities, e.g., $\nu_t/(U_c\delta)$ and $\alpha_t/(U_c\delta)$ for Newtonian jets, show an approximate plateau at $0 < y/\delta < 1$, as can be seen in Fig. 14 or from results from previous experimental studies [73–75]. For $y/\delta > 1$ the intermittent character of the positions of the turbulent/nonturbulent interfaces, of vorticity [76] and scalar gradient [77], with respect to the flow centerline invalidates the simple turbulent diffusivity model, even though the intermittent behavior of the interface can still be incorporated in turbulence models using different techniques [78–80].

At the initial large Deborah number region of the far field the influence of viscoelasticity is to decrease the values of the normalized ν_t and α_t, so as to attenuate large-scale stirring [Figs. 14(a) and 14(b)]. Furthermore, the hypothesis of a constant (normalized) eddy diffusivity is dubious for the highly viscoelastic cases, even at $0 < y/\delta < 1$ and specifically for the scalar transport. The turbulent Schmidt number at $0 < y/\delta < 1$ is clearly not constant for viscoelastic cases, except those with low elasticity. At the centerline Sc_t is increased by viscoelasticity but it decreases towards $y/\delta \approx 1$, where values that are lower than the Newtonian value can be observed. Lower values of normalized ν_t and α_t and larger Sc_t were also found at the outer layer of highly drag reduced turbulent flows between parallel plates [3,4]. These results suggest that the Reynolds analogy is not applicable to viscoelastic turbulent jets and wakes in the high De(x) region.

For large x distances, at the low elasticity region where viscoelastic effects become weaker, $\nu_t/\Delta U\delta$ of viscoelastic flows approach the Newtonian value, and may even be higher in some cases, whereas $\alpha_t/\Delta U\delta$ is larger for most cases, suggesting enhanced stirring of passive scalar at these farther regions (Appendix E). The exception is the wake flow case with the largest elasticity (Wi = 5, $1 - \beta = 0.10$, and $L = 200$). However, we expect the same behavior also for this case, but only much further downstream, at $x \gg 200d$.

IV. BUDGETS OF HALF SCALAR VARIANCE

For a steady mean flow the transport equation of the half scalar variance $\overline{\theta'^2}/2$ is given by

$$0 = -\frac{1}{2}\bar{u}_i\frac{\partial\overline{\theta'^2}}{\partial x_i} - \frac{1}{2}\frac{\partial\overline{u_i'\theta'^2}}{\partial x_i} + D\nabla^2\overline{\theta'^2}/2 - \overline{u_i'\theta'}\frac{\partial\bar{\theta}}{\partial x_i} - \varepsilon_\theta, \tag{13}$$

where $-(1/2)\bar{u}_i\partial\overline{\theta'^2}/\partial x_i$ is the advection term, $-(1/2)\partial\overline{u_i'\theta'^2}/\partial x_i$ is the turbulent diffusion term, $D\nabla^2\overline{\theta'^2}/2$ is the molecular diffusion term, $-\overline{u_i'\theta'}\partial\bar{\theta}/\partial x_i$ is the production term, and as before, $\varepsilon_\theta = D\overline{(\partial\theta'/\partial x_i')^2}$ is the mean rate of dissipation of half the scalar variance.

Transverse profiles of all terms of Eq. (13) are displayed in Fig. 15, at two different x/d stations, $x/d = 40$ and 120, for Newtonian and viscoelastic wakes with all terms normalized by $\Delta U\theta_c^2/\delta$. The budgets of the reference Newtonian wake are shown in Figs. 15(a) and 15(c), while

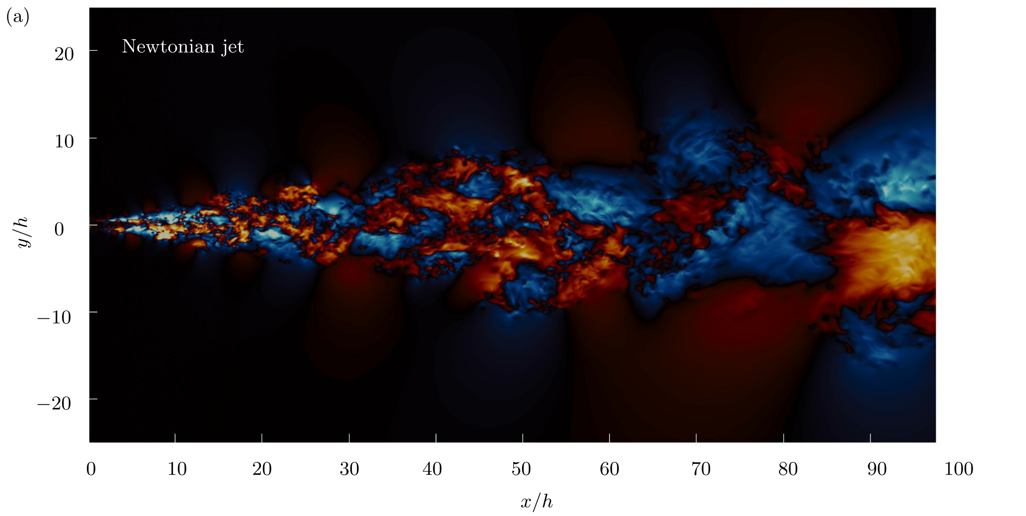

FIG. 12. Two-dimensional contours of the instantaneous streamwise velocity fluctuation $u' = u - \bar{u}$ at $z = 0$: (a) Newtonian jet at Re = 2500 and (b) viscoelastic jet at Re = 2500, Wi = 5, $1 - \beta = 0.02$, and $L = 200$. The same colormap range is used in both cases.

the viscoelastic results are shown in Figs. 15(b) and 15(d). The focus of Fig. 15(b) is on the high elasticity region of the flow, where the large-scale stirring of passive scalars is suppressed by the polymers, whereas the results for the low elasticity region, where the stirring of passive scalars is enhanced by viscoelasticity, are displayed in Fig. 15(d).

At $x/d = 40$, the turbulent scalar fluctuations at the centerline of the Newtonian wake are maintained predominantly by the advection promoted by the mean flow, and partially by the turbulent diffusion term, and this is balanced by dissipation at $y/\delta = 0$ [Fig. 15(a)]. The addition of polymers leads to dramatic changes, both qualitatively and quantitatively [Fig. 15(b)]. The variation of the advection term is so large that it even becomes a small sink at $y/\delta = 0$, even if for a short extent. The scalar fluctuation at the centerline ($y/\delta = 0$) is maintained predominantly by turbulent diffusion, which redistributes the scalar fluctuations that are produced at the shear layer region

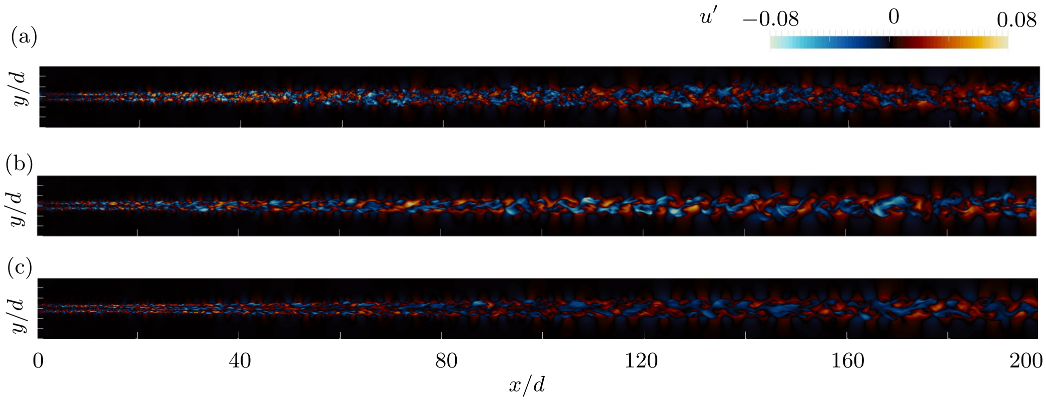

FIG. 13. Two-dimensional contours of the instantaneous streamwise velocity fluctuation $u' = u - \bar{u}$ at $z = 0$ for (a) Newtonian wake at $\mathrm{Re} = 2000$; (b) viscoelastic wake at $\mathrm{Re} = 2000$, $\mathrm{Wi} = 3$, $1 - \beta = 0.02$, and $L = 200$; and (c) viscoelastic wake at $\mathrm{Re} = 2000$, $\mathrm{Wi} = 5$, $1 - \beta = 0.10$, and $L = 200$.

($y/\delta \approx 0.5$) by the mean scalar gradient. The production term is reduced by viscoelasticity by as much as 75%, as are all the terms of the budget; its peak value moves closer to the centerline, but its overall shape is qualitatively similar to the Newtonian profile.

At station $x/d = 120$ the normalized scalar variance of the Newtonian wake has already reached a self-similar plateau, whereas viscoelasticity promoted an enhancement of the centerline turbulent scalar fluctuations [Fig. 2(b)]. For the Newtonian wake, the scalar fluctuations at the centerline are maintained mainly by the turbulent diffusion term, and partially by the advection term, which are approximately balanced by the dissipation at $y/\delta = 0$ [Fig. 15(c)]. In contrast, the centerline scalar fluctuations of the viscoelastic wake at this low elasticity region are maintained predominantly by mean flow advection, which is considerably larger than the turbulent diffusion term, and these terms are balanced by dissipation at $y/\delta = 0$ [Fig. 15(d)]. In this low elasticity region, the production and turbulent diffusion terms are also affected by viscoelasticity, but not so strongly as other terms. Similar results were observed for jets (Appendix E).

As mentioned before, the scalar dissipation profiles shown in Fig. 15(d) are normalized by $\Delta U \theta_c^2/\delta$, i.e., mean flow quantities. Comparing Figs. 15(c) and 15(d), it can be seen that the dissipation is much larger in the viscoelastic case and this is a consequence of the scaling because, from the analysis given in Sec. III B, it is clear that small-scale mixing is reduced by viscoelasticity.

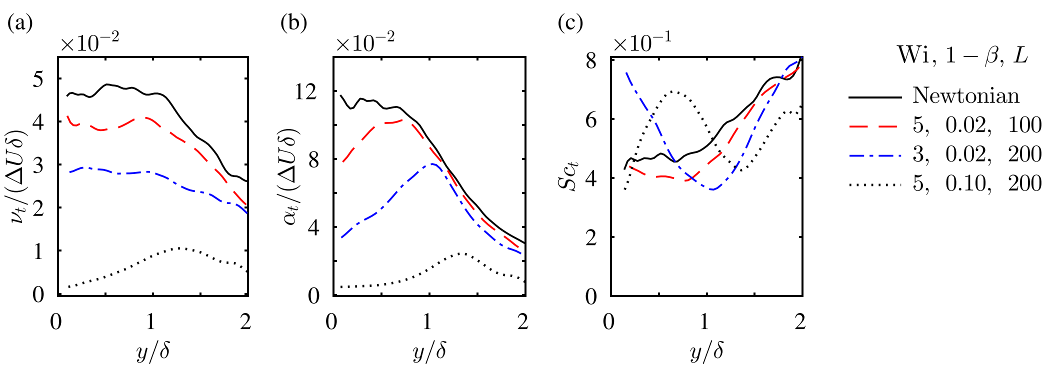

FIG. 14. Transverse profiles of the normalized turbulent diffusivity of momentum (a), scalar (b), and turbulent Schmidt number (c) for wakes at $x/d = 80$. Data from jet simulations are shown in Appendix E.

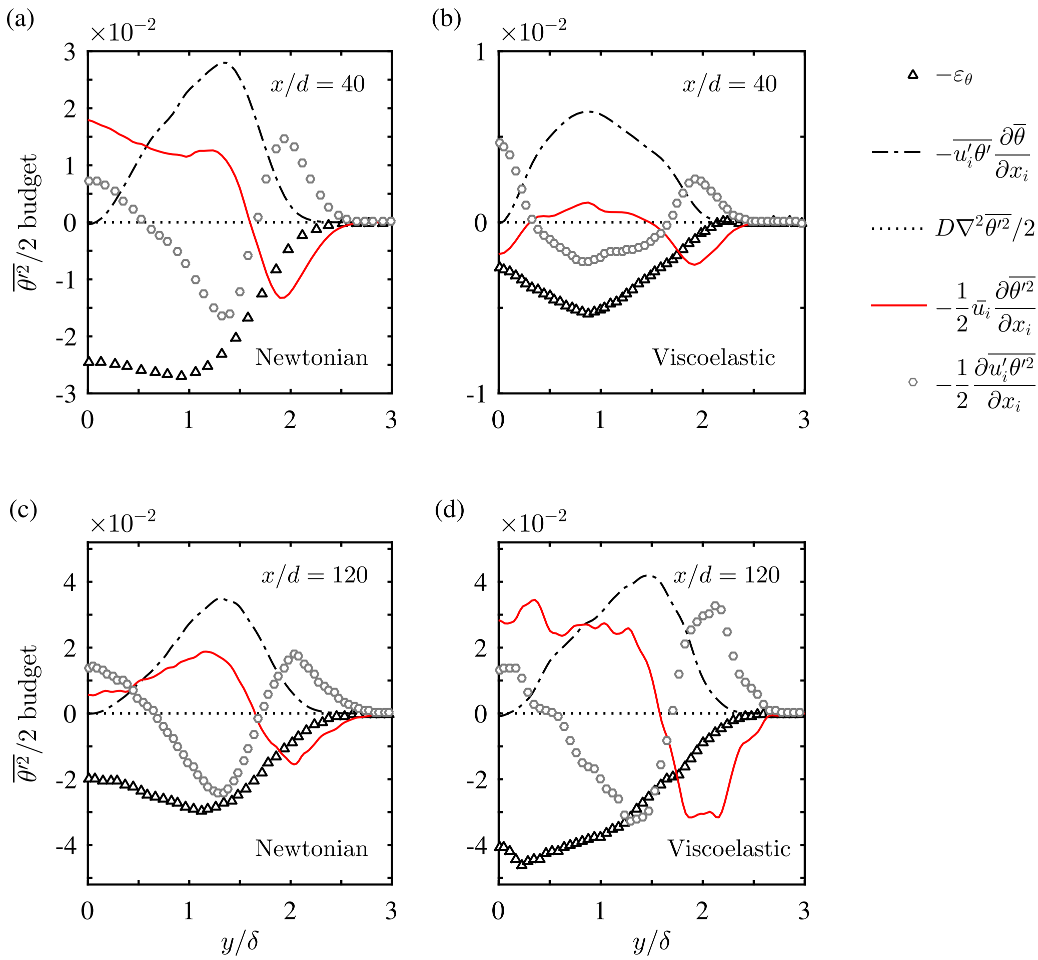

FIG. 15. Budgets of scalar variance for (a),(c) Newtonian wake and (b),(d) viscoelastic wake with Wi $= 3$, $1 - \beta = 0.02$, and $L = 200$. The transverse profiles are shown at two different stations: (a),(b) $x/d = 40$ and (c),(d) $x/d = 120$. All terms are normalized by $\Delta U \theta_c^2/\delta$. Notice the different scales used at the ordinates of the plots.

This emphasizes that estimates of small-scale mixing based on the scalar dissipation rate need to be carried out with the correct scaling of the dissipation, based on turbulent flow quantities: $\varepsilon_\theta/(\sqrt{\kappa_c}\overline{\theta'^2}_c/\delta)$.

The influence of viscoelasticity on the budgets of half scalar variance at both low and high elasticity regions is qualitatively similar to that observed for the budgets of turbulent kinetic energy, investigated by Guimarães *et al.* [9], therefore suggesting a similar mechanism for the transfer of scalar variance and turbulent kinetic energy also for the viscoelastic cases. The nonuniform turbulent Schmidt numbers found at $0 < y/\delta < 1$ for highly viscoelastic flows and the resulting inadequacy of the Reynolds analogy must then be a consequence of the different degrees of sensitivity that the scalar and velocity fields have in relation to viscoelasticity.

V. CONCLUSIONS

Direct numerical simulations of spatially evolving turbulent planar jets and wakes were performed in order to study the mixing of passive scalars in free turbulent shear flows of viscoelastic polymer solutions. The DNSs are based on the FENE-P rheological model, and on a highly accurate numerical code [8,44] that employs pseudospectral/sixth-order compact finite differences and the shock-capturing scheme of Kurganov and Tadmor [51,52].

Viscoelasticity has a strong influence on the evolution of the passive scalar field. Small-scale mixing is suppressed, while large- and intermediate-scale stirring can be suppressed or enhanced depending on the flow region and rheological parameters of the fluid. At the near field, in the high elasticity region, stirring is suppressed by viscoelasticity leading to a substantial decrease of the spreading and decay rates of the passive scalar and a suppression of the normalized passive scalar variance. In contrast, at the low elasticity region of the very distant far field, the suppression of the small-scale mixing is compensated by an increase of the large-scale stirring, resulting in larger spreading and decay rates and higher values of the normalized scalar variance.

The explanation for this behavior is the suppression of the small-scale turbulent motions caused by the polymers, resulting in smaller isoscalar surface areas (less corrugated isosurfaces) and therefore smaller mixing rates, and enlarged coherent structures that promote the stirring of passive scalars at the large scales.

Even though some similarities between the transport of momentum and scalar have been found for the viscoelastic flows considered here, the sensitivity of the scalar field to viscoelasticity is more pronounced and the consequence is that the Reynolds analogy ceases to be valid for turbulent viscoelastic jets and wakes at the high elasticity region.

ACKNOWLEDGMENTS

M.C.G. acknowledges funding from the Portuguese Fundação para a Ciência e Tecnologia (FCT) through Contract No. UI/BD/151060/2021. C.B.S. acknowledges funding from Fundação para a Ciência e Tecnologia (FCT) through IDMEC, under LAETA, Project No. UIDB/50022/2020. F.T.P. is thankful for funding by FCT and Centro de Estudos de Fenómenos de Transporte through Projects No. UIDB/00532/2020 and No. UIDP/00532/2020, and for funding by FCT and ALiCE through Project No. LA/P/0045/2020.

APPENDIX A: MESH RESOLUTION STUDY

The resolution of the simulations presented in the core of the paper was verified by comparing them to DNSs that use different grid spacing Δx. Due to computational constraints, a smaller computational domain was used for some cases. In these comparisons, all parameters are kept unchanged except for the number of grid points on each spatial direction.

For each simulation, the grid spacing normalized by the Kolmogorov length scale $\Delta x/\eta$ reaches its maximum value ($\max|\Delta x/\eta|$) at the end of the transition region and decays at the fully turbulent far far-field; maximum and far-field values have been listed in Table I. Thus, to properly verify the mesh resolution it is important to use computational domains that are large enough to cover the position where $\max|\Delta x/\eta|$ is reached. All simulations presented in this appendix verify this condition. In fact, they use computational domains that are actually larger so that the fully turbulent far field is also covered.

It is demonstrated here that the simulations analyzed in the core of the paper use meshes that are sufficiently fine. For most turbulence statistics these DNSs use meshes that are actually finer than necessary, since the same results can be obtained from coarser simulations. For instance, with the numerical methods adopted here (see Sec. II B), statistics such as the spreading and decay rates of the mean velocity, the Reynolds stresses, the normalized scalar variance, and some other quantities are well captured if $\max|\Delta x/\eta| \lesssim 5$, whereas the decay rate of the mean passive scalar needs a higher resolution to be properly captured. The values of the resolution parameter $\max|\Delta x/\eta|$ required for the different cases are (i) $\max|\Delta x/\eta| \lesssim 3.3$ and 2.8, for Newtonian jets at $\mathrm{Re} = 3500$ and 2500, respectively; (ii) $\max|\Delta x/\eta| \lesssim 3.5$ and 4.7, for viscoelastic jets at $\mathrm{Re} = 3500$ and 2500, respectively; (iii) $\max|\Delta x/\eta| \lesssim 2.5$ for Newtonian wakes at $\mathrm{Re} = 2000$; and (iv) $\max|\Delta x/\eta| \lesssim 1.6$ for

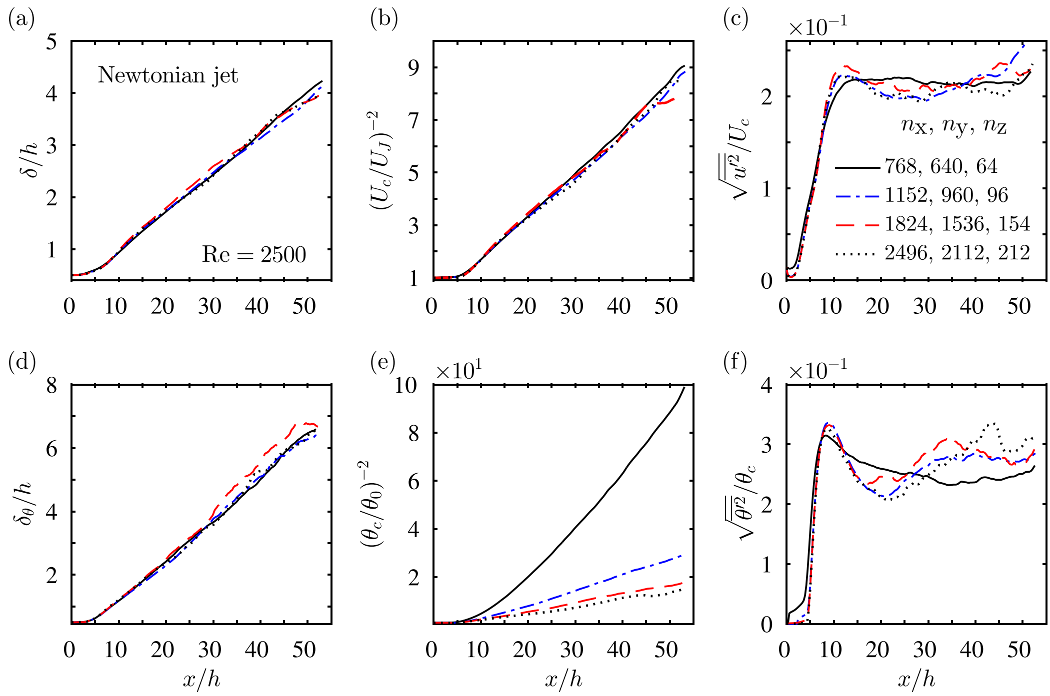

FIG. 16. Streamwise evolution of normalized statistics from four DNSs of Newtonian jets with Re = 2500, that use a different number of grid points on each direction, n_x, n_y, and n_z, assessing the influence of mesh resolution on the results: (a) jet half-width, (b) centerline mean velocity, (c) centerline streamwise velocity fluctuation, (d) scalar half-width, (e) mean scalar on the centerline, and (f) centerline scalar variance. The sizes of the computational domains are $L_x = 53.33h$, $L_y = 44.44h$, and $L_z = 4.44h$. The grid spacings normalized by the Kolmogorov length scale of each simulation are $\max|\Delta x/\eta| = 6.7,\ 4.5, 2.8$, and 2.0, ordered from the coarsest to the finest mesh.

viscoelastic wakes at Re = 2000. The DNS data that support these conclusions are displayed in Figs. 16–21. The physical and computational parameters of the DNSs presented in those figures are described in the captions and legends of the figures.

APPENDIX B: VALIDATION OF THE SIZES OF THE COMPUTATIONAL DOMAINS

This validation was carried out through the comparison between the results obtained from DNSs that use different sizes of the computational domain. Four cases were considered: (i) Newtonian jet at Re = 2500; (ii) viscoelastic jet at Re = 2500, Wi = 5, $L = 200$, and $1 - \beta = 0.02$; (iii) Newtonian wake at Re = 2000; and (iv) viscoelastic wake at Re = 2000, Wi = 3, $L = 200$, and $1 - \beta = 0.02$. These are the simulations that were already described in the main body of the paper and in Appendix A. The results, displayed in Figs. 22–25, confirm that the simulations use computational domain sizes that are sufficiently large to allow the normal development of the flow.

APPENDIX C: REYNOLDS NUMBER EFFECTS

This Appendix compares the reference Newtonian simulations used in the core of the paper with new simulations at larger Reynolds numbers Re, in order to study the effect of Re on the turbulence statistics. Due to the high computational cost of the simulations, the DNSs at larger Re

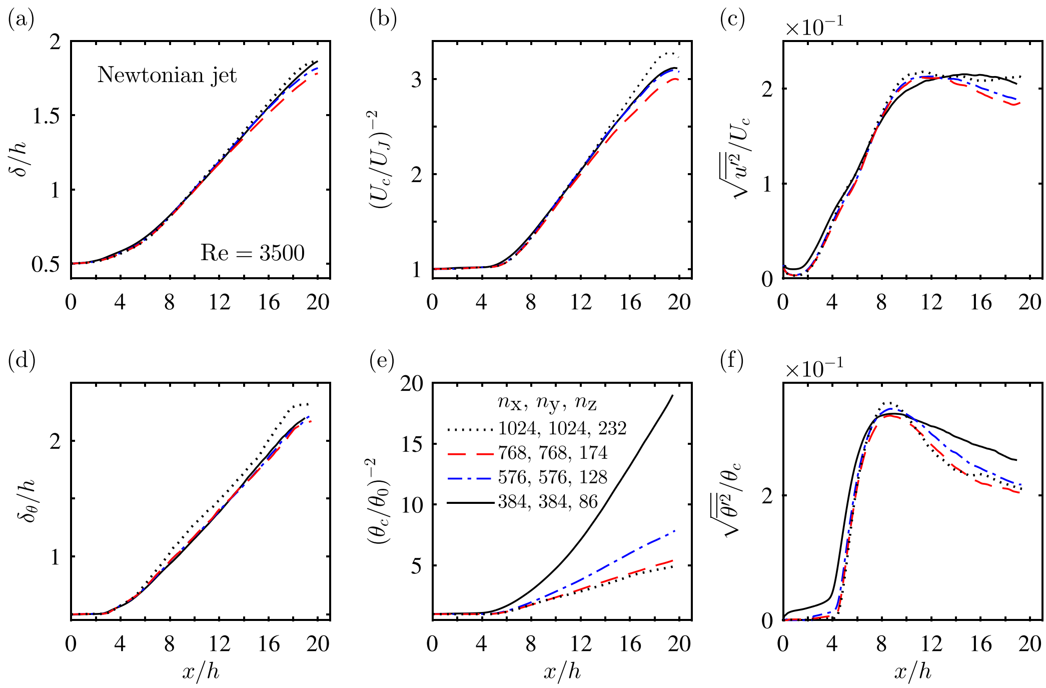

FIG. 17. Streamwise evolution of normalized statistics from four DNSs of Newtonian jets with Re $= 3500$, that use a different number of grid points on each direction, n_x, n_y, and n_z, assessing the influence of mesh resolution on the results: (a) jet half-width, (b) centerline mean velocity, (c) centerline streamwise velocity fluctuation, (d) scalar half-width, (e) mean scalar on the centerline, and (f) centerline scalar variance. The sizes of the computational domains are $L_x = L_y = 20h$ and $L_z = 4.5h$. The grid spacings normalized by the Kolmogorov length scale of each simulation are, $\max|\Delta x/\eta| = 6.4,\ 4.3,\ 3.3$ and 2.5, ordered from the coarsest to the finest mesh.

were performed with smaller computational domains, and this study was carried out for Newtonian flows only.

The new DNSs are as follows: (i) planar jet with Re $= 3500$, $L_x/h = 40.5$, $L_y/h = 36$, $L_z/h = 4.5$, $n_x = 1152$, $n_y = 1024$, $n_z = 128$, $\max|\Delta x/\eta| = 4.4$, and $\mathrm{Re}_\lambda = 128$ and (ii) planar wake with Re $= 4000$, $L_x/d = 120$, $L_y/d = 20$, $L_z/d = 5$, $n_x = 3456$, $n_y = 576$, $n_z = 144$, $\max|\Delta x/\eta| = 4.7$, and $\mathrm{Re}_\lambda = 108$. In Appendix A it was demonstrated that this level of mesh resolution, in terms of the parameter $\max|\Delta x/\eta|$, is high enough to capture the evolution of several statistics, such as δ/h, U_c/U_J, $\Delta U/U_\infty$, $\sqrt{\overline{u'^2}}/U_c$, δ_θ/h, and $\sqrt{\overline{\theta'^2}}/\theta_c$. The comparisons presented here are based on these statistics. The decay rate of the mean passive scalar at the centerline requires a higher resolution (Appendix A) and therefore we will use the Newtonian jet DNS at Re $= 3500$ and a smaller domain size with a higher resolution, listed in Table I, to compute the decay rate of the passive scalar of the jet at this relatively higher Reynolds number.

Comparisons between the turbulence statistics obtained from flows at different Reynolds numbers are shown in Figs. 26 and 27, for jets and wakes, respectively. In both cases, the effect of Re is small and the statistics obtained from flows at different Re are nearly indistinguishable. The normalized velocity and passive scalar fluctuations show a Reynolds number dependence at the far field, but only at the quantitative level and nevertheless the dependence is very small. The decay rate of the passive scalar of the jet is not very sensitive to Re, with $A_{\theta_c} = 0.32$ and 0.28, for Re $= 2500$ and 3500, respectively (not shown in the figures).

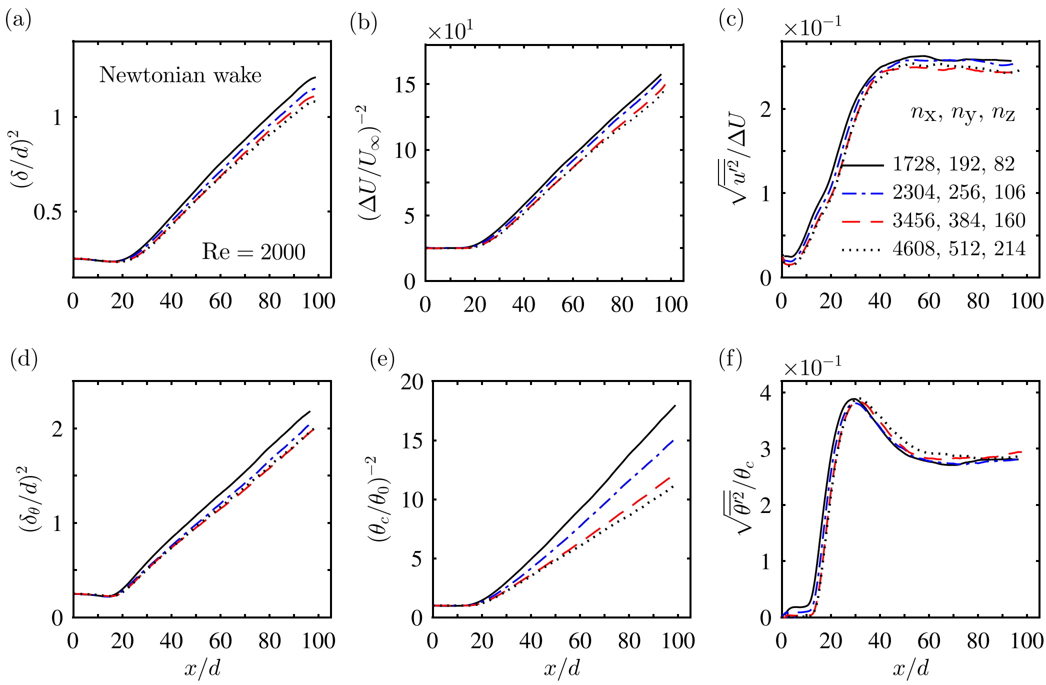

FIG. 18. Streamwise evolution of normalized statistics from four DNSs of Newtonian wakes with Re = 2000, that use a different number of grid points on each direction, n_x, n_y, and n_z, assessing the influence of mesh resolution on the results: (a) wake half-width, (b) centerline mean velocity deficit, (c) centerline streamwise velocity fluctuation, (d) scalar half-width, (e) mean scalar on the centerline, and (f) centerline scalar variance. The sizes of the computational domains are $L_x = 99d$, $L_y = 11d$, and $L_z = 4.6d$. The grid spacings normalized by the Kolmogorov length scale of each simulation are, $\max|\Delta x/\eta| = 4.8,\ 3.7,\ 2.5$ and 1.9, ordered from the coarsest to the finest mesh.

APPENDIX D: VALIDATION OF THE DNS CODE

The numerical code was extensively validated through comparisons with experimental and numerical data from the literature, for both laminar, transitioning and fully turbulent regimes. Several results have already been shown and discussed in previous references [8,9,44–46], and here we show some additional comparisons with numerical and experimental data from the literature that complement the previous validation studies.

For planar wakes, transverse profiles at different x stations for several passive scalar turbulence statistics are compared in Fig. 28 with the experimental data of Townsend [81], Freymuth and Uberoi [82], LaRue and Libby [83], Fabris [84], Antonia and Browne [74,85], Browne and Antonia [86], Rehab *et al.* [87], Kang and Meneveau [88] and Mi *et al.* [89]. For planar jets, the profiles are compared in Fig. 29 with the experimental data of van der Hegge Zijnen [90], Jenkins and Goldschmidt [91], Antonia *et al.* [92], Ramaprian and Chandrasekhara [93], Watanabe *et al.* [94] and Terashima *et al.* [95] and the numerical data of Wu *et al.* [96] and Watanabe *et al.* [61].

In the far-field region of the jet/wake, the profiles of mean passive scalar are virtually the same in all experimental and numerical works. Some quantitative differences can be observed between different data sets for the profiles of the remaining statistics. This confirms the well-known lack of universality that exists between flows with distinct inlet/initial conditions. Nevertheless, the results confirm that the data from our simulations are in very good agreement with experimental and numerical data from the literature and, similarly to our previous works [8,9,44–46], validate the present DNSs of jets and wakes.

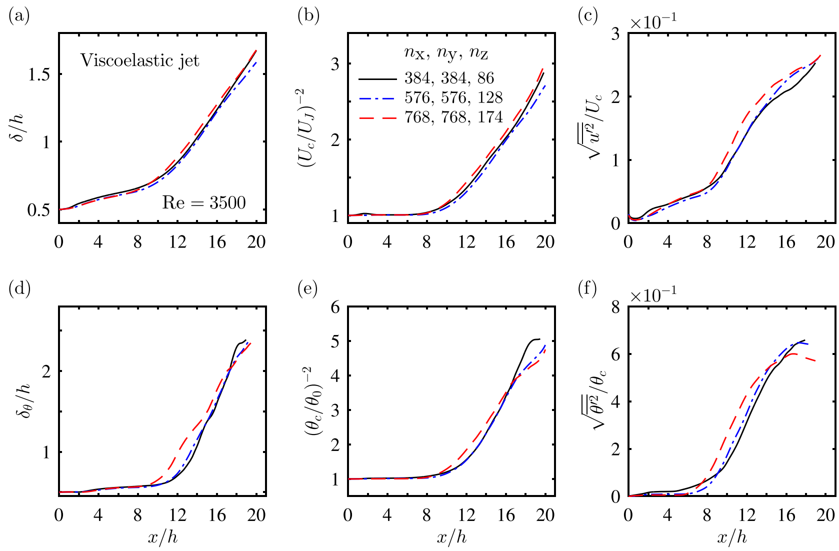

FIG. 19. Streamwise evolution of normalized statistics from three DNSs of viscoelastic jets with Re = 3500, Wi = 3, $L = 100$, and $1 - \beta = 0.2$, that use a different number of grid points on each direction, n_x, n_y, and n_z, assessing the influence of mesh resolution on the results: (a) jet half-width, (b) centerline mean velocity, (c) centerline streamwise velocity fluctuation, (d) scalar half-width, (e) mean scalar on the centerline, and (f) centerline scalar variance. The sizes of the computational domains are $L_x = 20h$, $L_y = 20h$, and $L_z = 4.5h$. The grid spacings normalized by the Kolmogorov length scale of each simulation are $\max|\Delta x/\eta| = 3.5,\ 2.4$, and 1.9, ordered from the coarsest to the finest mesh.

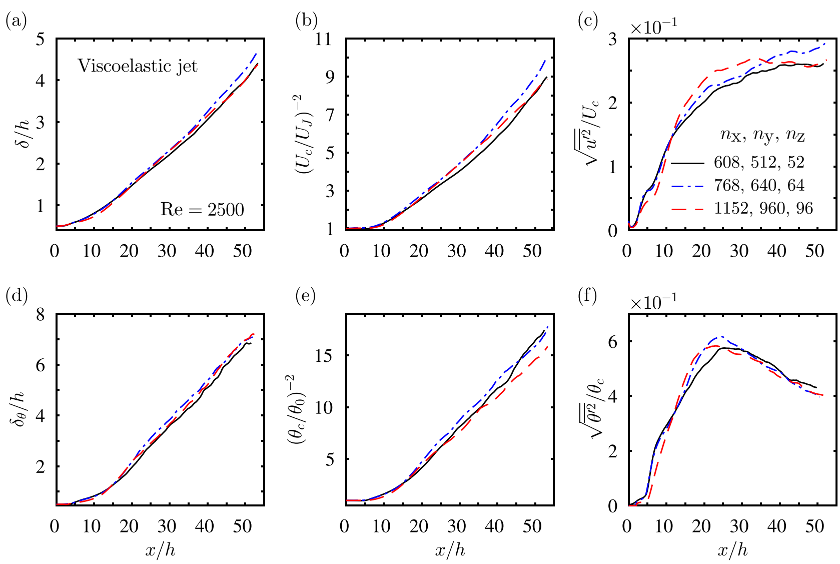

FIG. 20. Streamwise evolution of normalized statistics from three DNSs of viscoelastic jets with Re = 2500, Wi = 5, $L = 200$, and $1 - \beta = 0.02$, that use a different number of grid points on each direction, n_x, n_y, and n_z, assessing the influence of mesh resolution on the results: (a) jet half-width, (b) centerline mean velocity, (c) centerline streamwise velocity fluctuation, (d) scalar half-width, (e) mean scalar on the centerline, and (f) centerline scalar variance. The sizes of the computational domains are $L_x = 53.33h$, $L_y = 44.44h$, and $L_z = 4.44h$. The grid spacings normalized by the Kolmogorov length scale of each simulation are $\max|\Delta x/\eta| = 4.7,\ 3.7$, and 2.6, ordered from the coarsest to the finest mesh.

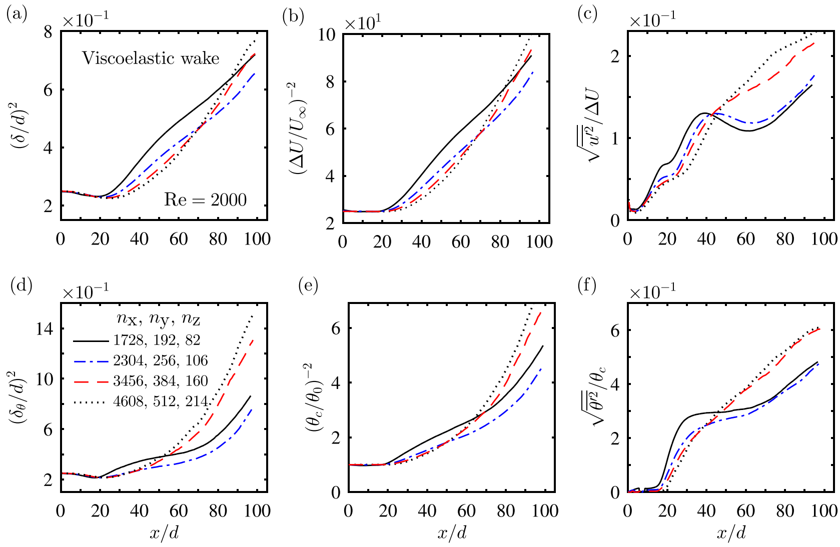

FIG. 21. Streamwise evolution of normalized statistics from four DNSs of viscoelastic wakes with Re $=$ 2000, Wi $= 3$, $L = 200$, and $1 - \beta = 0.02$, that use a different number of grid points on each direction, n_x, n_y, and n_z, assessing the influence of mesh resolution on the results: (a) wake half-width, (b) centerline mean velocity deficit, (c) centerline streamwise velocity fluctuation, (d) scalar half-width, (e) mean scalar on the centerline, and (f) centerline scalar variance. The sizes of the computational domains are $L_x = 99d$, $L_y = 11d$, and $L_z = 4.6d$. The grid spacings normalized by the Kolmogorov length scale of each simulation are $\max|\Delta x/\eta| = 3.2,\ 2.4, 1.6$, and 1.2, ordered from the coarsest to the finest mesh.

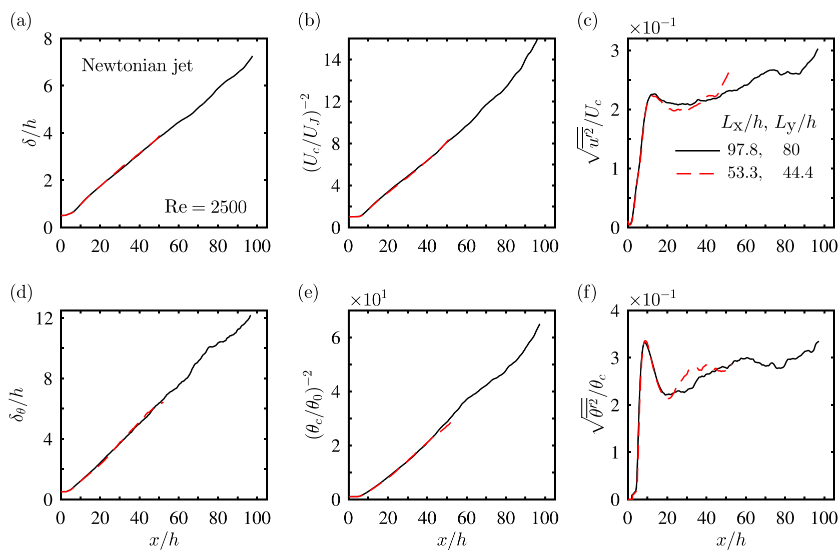

FIG. 22. Streamwise evolution of normalized statistics from two DNSs of Newtonian jets with Re $= 2500$, that use different sizes of the computational domain, L_x and L_y, with a fixed $L_z/h = 4.44$: (a) jet half-width, (b) centerline mean velocity, (c) centerline streamwise velocity fluctuation, (d) scalar half-width, (e) mean scalar on the centerline, and (f) centerline scalar variance. The grid spacing normalized by the Kolmogorov length scale of both simulations is $\max|\Delta x/\eta| = 4.5$. Note that the decay rate of the mean passive scalar, depicted in panel (e), is overestimated by these DNSs at $\max|\Delta x/\eta| = 4.5$, as demonstrated in our mesh resolution study presented in Appendix A.

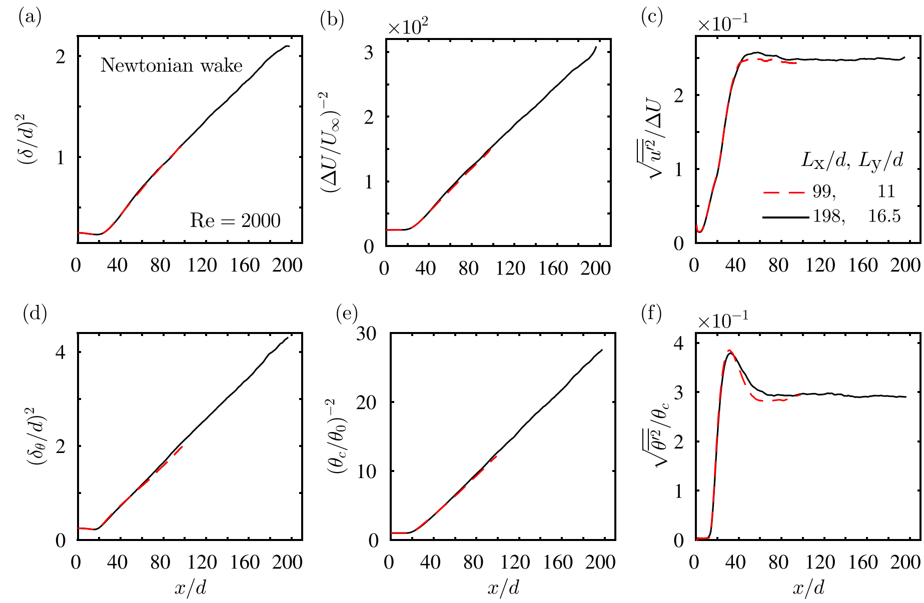

FIG. 23. Streamwise evolution of normalized statistics from two DNSs of Newtonian wakes with Re = 2000, that use different sizes of the computational domain, L_x and L_y, with a fixed $L_z/d = 4.55$: (a) wake half-width, (b) centerline mean velocity deficit, (c) centerline streamwise velocity fluctuation, (d) scalar half-width, (e) mean scalar on the centerline, and (f) centerline scalar variance. The grid spacing normalized by the Kolmogorov length scale of both simulations is $\max|\Delta x/\eta| = 2.5$.

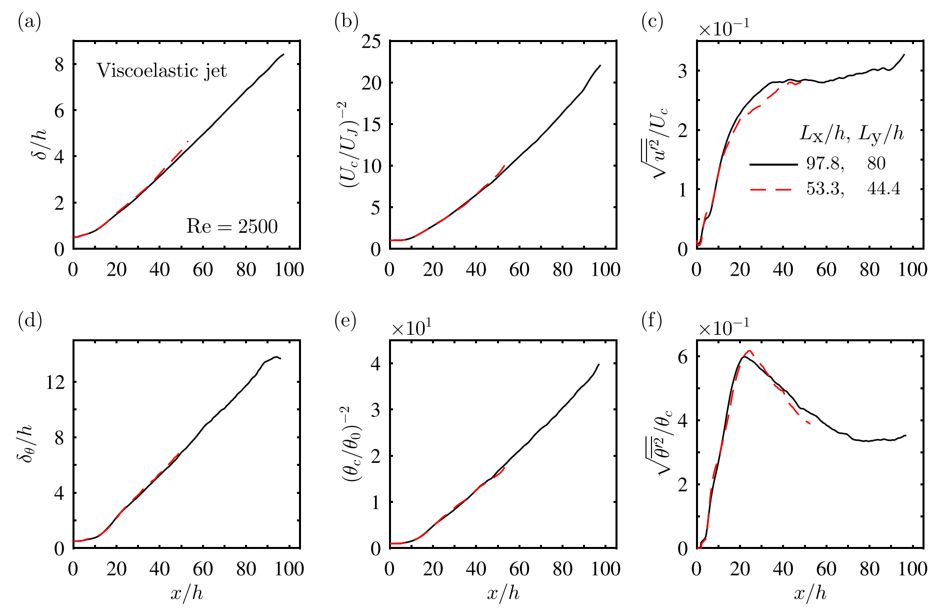

FIG. 24. Streamwise evolution of normalized statistics from two DNSs of viscoelastic jets with Re = 2500, Wi = 5, $L = 200$, and $1 - \beta = 0.02$, that use different sizes of the computational domain, L_x and L_y, with a fixed $L_z/h = 4.44$: (a) jet half-width, (b) centerline mean velocity, (c) centerline streamwise velocity fluctuation, (d) scalar half-width, (e) mean scalar on the centerline, and (f) centerline scalar variance. The grid spacing normalized by the Kolmogorov length scale of both simulations is $\max|\Delta x/\eta| = 3.7$.

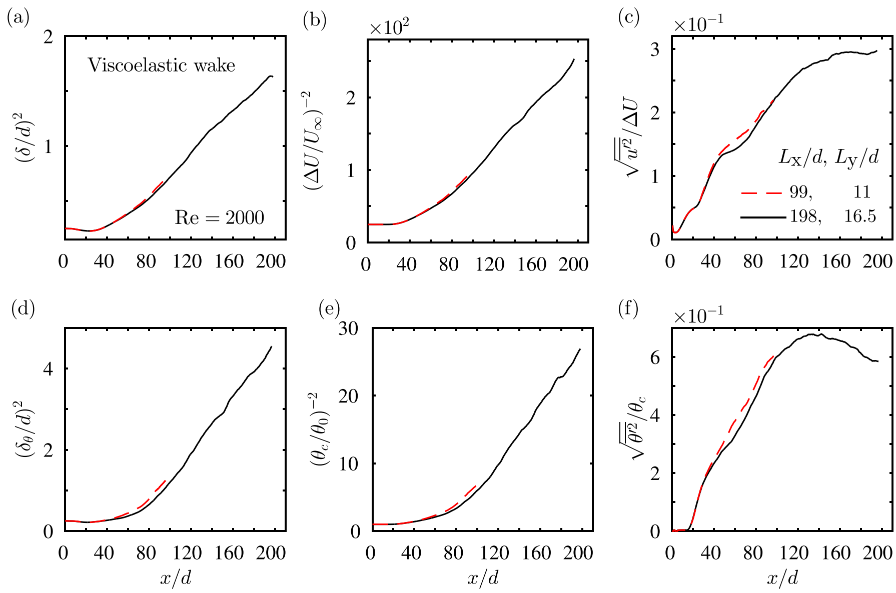

FIG. 25. Streamwise evolution of normalized statistics from two DNSs of viscoelastic wakes with Re = 2000, Wi = 3, $L = 200$, and $1 - \beta = 0.02$, that use different sizes of the computational domain, L_x and L_y, with a fixed $L_z/d = 4.55$: (a) wake half-width, (b) centerline mean velocity deficit, (c) centerline streamwise velocity fluctuation, (d) scalar half-width, (e) mean scalar on the centerline, and (f) centerline scalar variance. The grid spacing normalized by the Kolmogorov length scale of both simulations is $\max|\Delta x/\eta| = 1.6$.

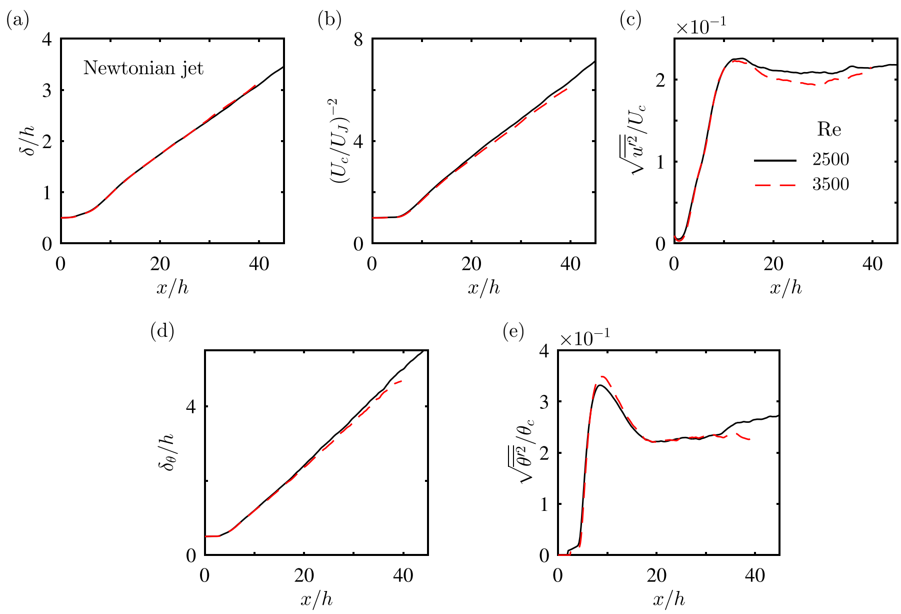

FIG. 26. Streamwise evolution of normalized statistics from two DNSs of Newtonian jets with different values of the inlet Reynolds number: (a) jet half-width, (b) centerline mean velocity, (c) centerline streamwise velocity fluctuation, (d) scalar half-width, and (e) centerline scalar variance. The grid spacing normalized by the Kolmogorov length scale of the simulations are $\max|\Delta x/\eta| = 4.5$ and 4.4, for a Re_λ at $x/h = 35$ equal to 111 and 128, for the jets with Re = 2500 and 3500, respectively.

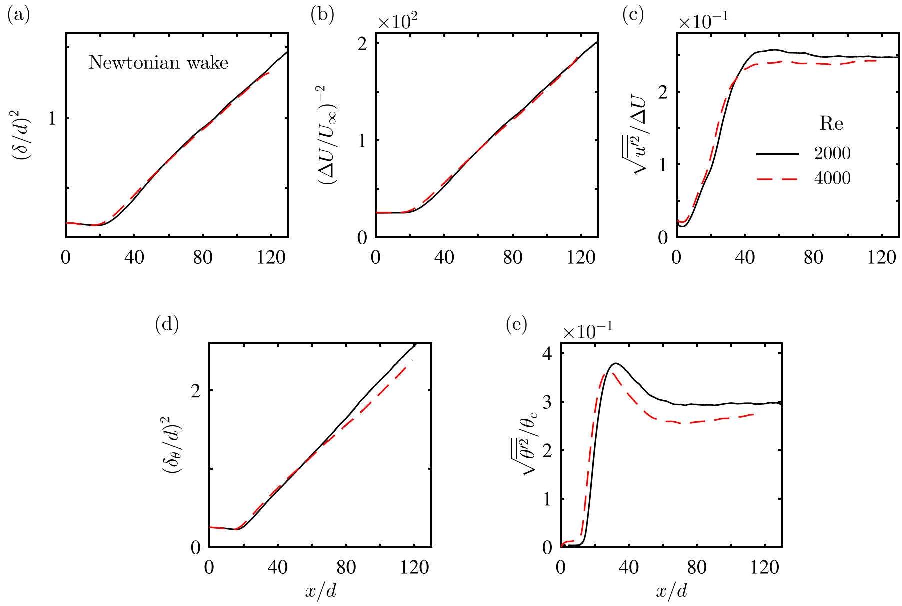

FIG. 27. Streamwise evolution of normalized statistics from two DNSs of Newtonian jets with different values of the inlet Reynolds number: (a) wake half-width, (b) centerline mean velocity deficit, (c) centerline streamwise velocity fluctuation, (d) scalar half-width, and (e) centerline scalar variance. The grid spacing normalized by the Kolmogorov length scale of the simulations are max$|\Delta x/\eta|$ = 2.5 and 4.7 and $\mathrm{Re}_\lambda = 64$ and 108, for the jets with Re = 2000 and 4000, respectively.

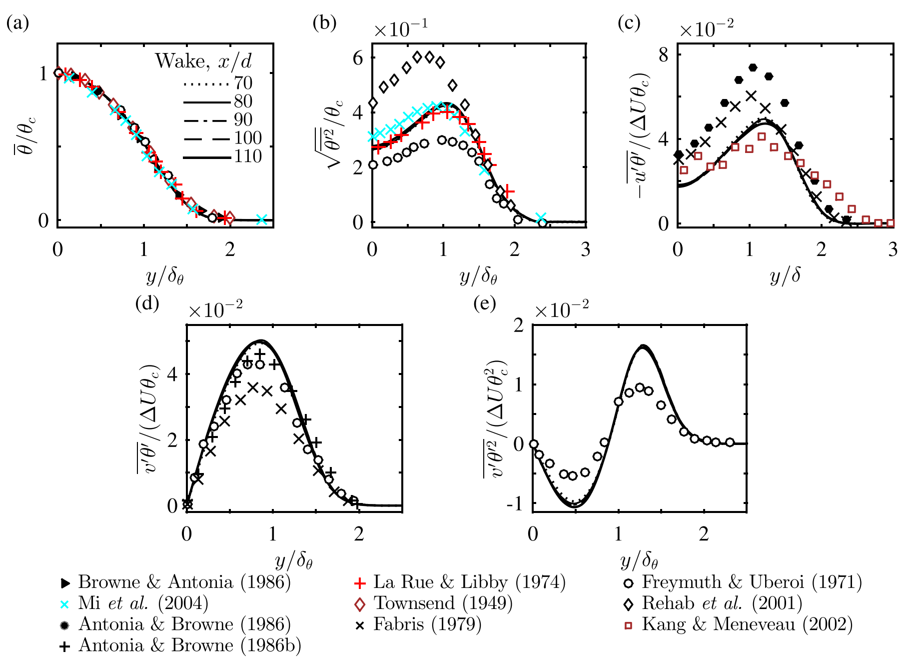

FIG. 28. Transverse profiles of several normalized turbulence statistics at different x/d stations, from the Newtonian wake DNS with Re = 4000. The results are compared against experimental data from the literature. The legend for the profiles from the DNS is shown in panel (a).

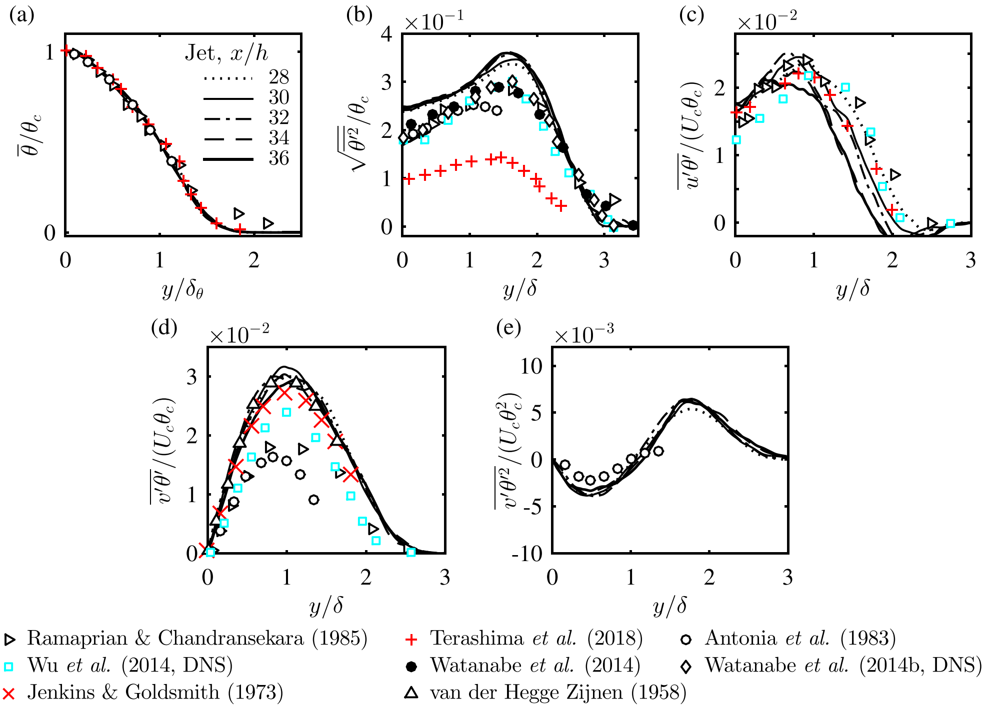

FIG. 29. Transverse profiles of several normalized turbulence statistics at different x/h stations, from the Newtonian jet DNS with Re = 3500. The results are compared against experimental and numerical data from the literature. The legend for the profiles from the DNS is shown in panel (a).

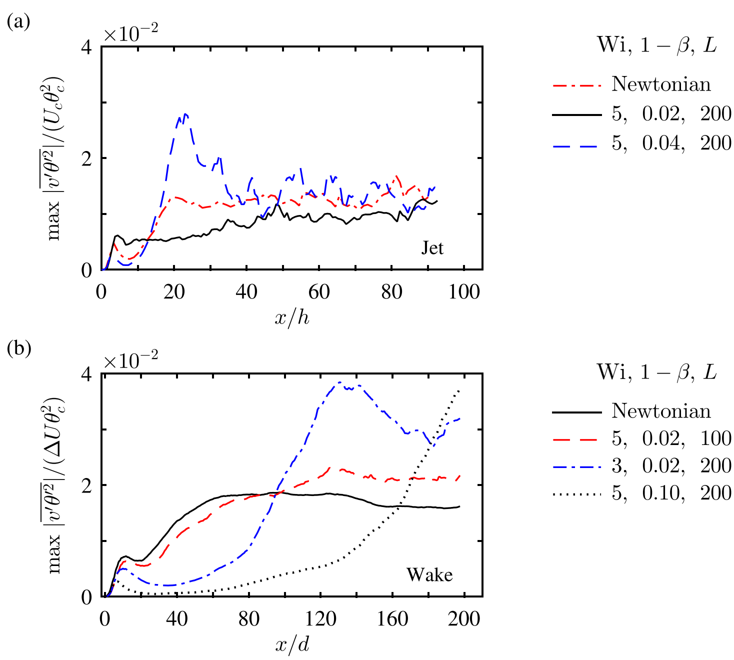

FIG. 30. Streamwise evolution of the normalized turbulent flux of scalar variance for jets (a) and wakes (b).

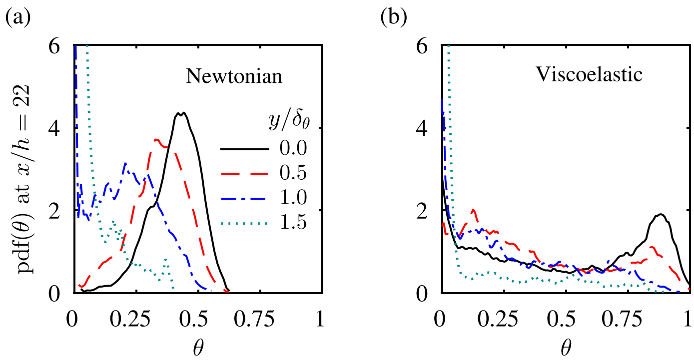

FIG. 31. Scalar probability density function distribution at four y/δ_θ positions at $x/h = 22$ for (a) Newtonian jet and (b) viscoelastic jet with Wi $= 5$, $1 - \beta = 0.04$, and $L = 200$. The Reynolds number is Re $= 2500$. For the Newtonian jet, the results from the DNS at the highest resolution are shown.

APPENDIX E: COMPLEMENTARY DATA

This appendix shows the data that was omitted from the core of the paper to enhance its readability. The data are displayed in Figs. 30–35.

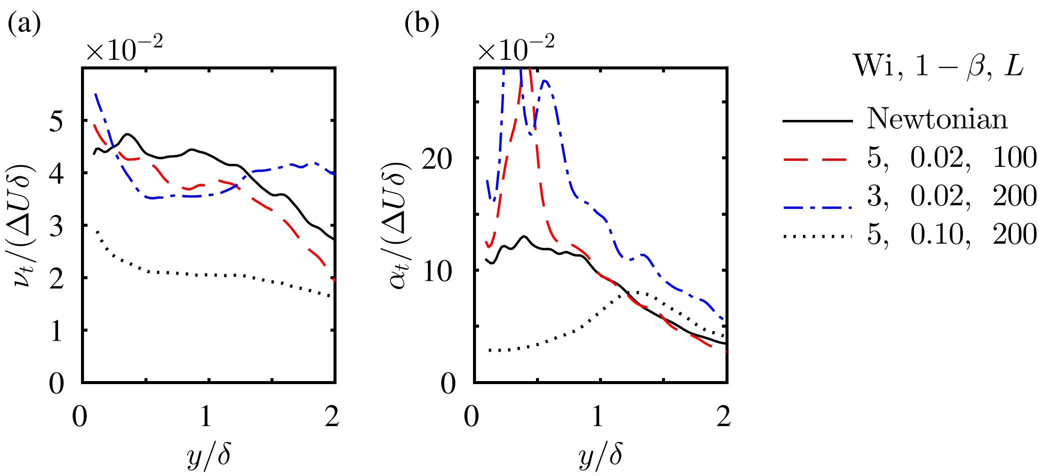

FIG. 32. Transverse profiles of the normalized turbulent diffusivity of momentum (a) and scalar (b) for wakes at $x/d = 160$.

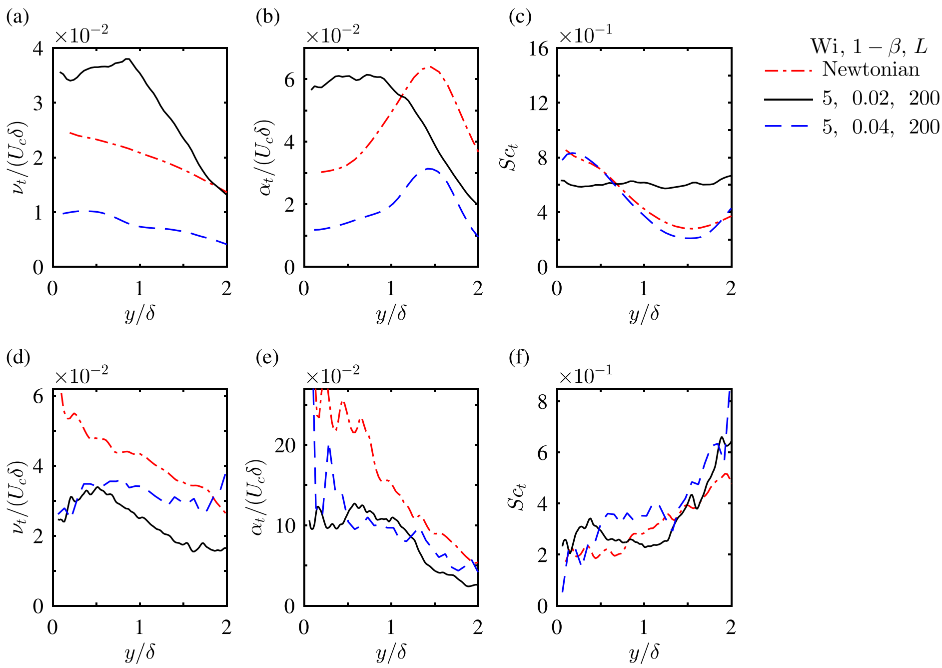

FIG. 33. Transverse profiles of the normalized turbulent diffusivity of momentum (a),(d), scalar (b),(e), and turbulent Schmidt number (c),(f) for jets at $x/h = 12$ (a)–(c) and $x/h = 40$ (d)–(f).

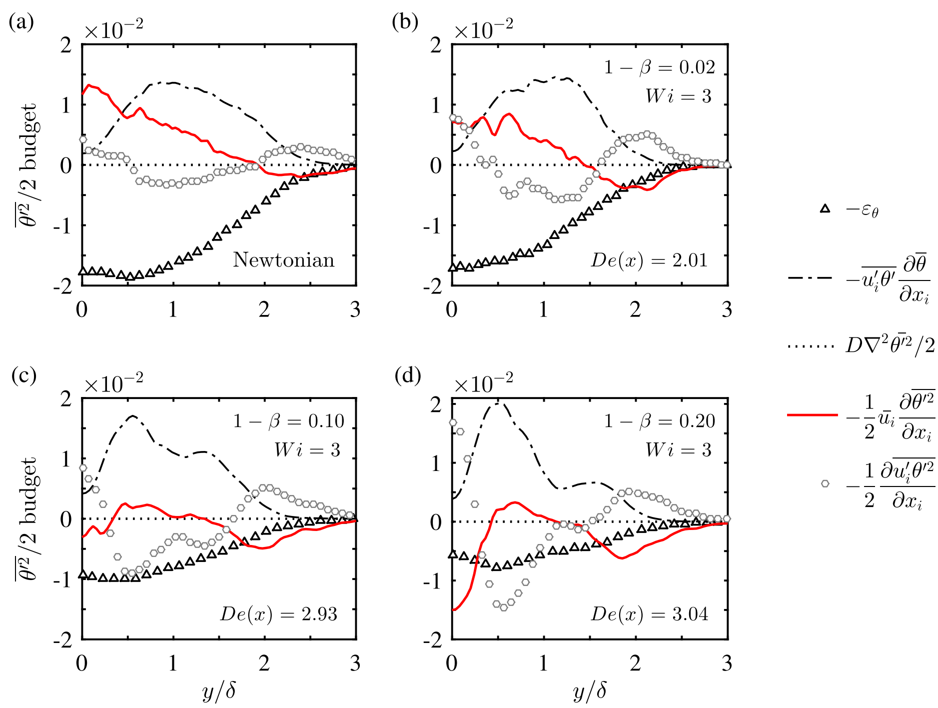

FIG. 34. Budgets of half scalar variance at $x/h = 12$ for (a) Newtonian jet with Re = 3500 and (b)–(d) viscoelastic jets with Re = 3500 and $L = 100$ at the high elasticity region. All terms are normalized by $U_c\theta_c^2/\delta$.

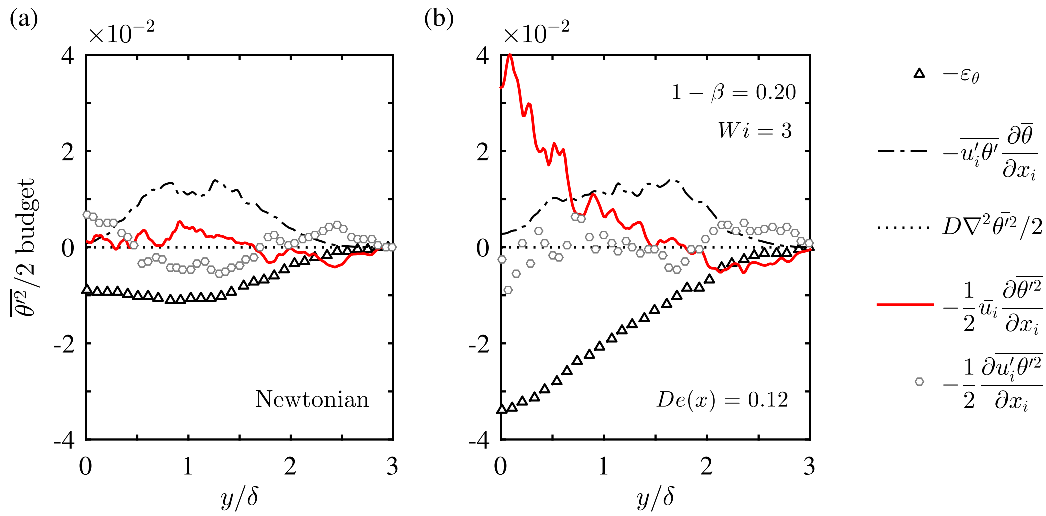

FIG. 35. Budgets of half scalar variance at $x/h = 25$ for (a) Newtonian jet with Re = 3500 and (b) viscoelastic jet with Re = 3500 and $L = 100$ at the low elasticity region. All terms are normalized by $U_c\theta_c^2/\delta$.

[1] E. F. Matthys, Heat transfer, drag reduction, and fluid characterization for turbulent flow of polymer solutions: Recent results and research needs, J. Non-Newtonian Fluid Mech. **38**, 313 (1991).
[2] R. H. J. Sellin, J. W. Hoyt, J. Poliert, and O. Scrivener, The effect of drag reducing additives on fluid flows and their industrial applications part 2: Present applications and future proposals, J. Hydraul. Res. **20**, 235 (1982).
[3] V. K. Gupta, R. Sureshkumar, and B. Khomami, Passive scalar transport in polymer drag-reduced turbulent channel flow, AIChE J. **51**, 1938 (2005).
[4] K. Kim and R. Sureshkumar, Effects of polymer stresses on analogy between momentum and heat transfer in drag-reduced turbulent channel flow, Phys. Fluids **30**, 035106 (2018).
[5] C. D. Dimitropoulos, Y. Dubief, E. S. G. Shaqfeh, and P. Moin, Direct numerical simulation of polymer-induced drag reduction in turbulent boundary layer flow of inhomogeneous polymer solutions, J. Fluid Mech. **566**, 153 (2006).
[6] D. Richter, E. S. G. Shaqfeh, and G. Iaccarino, Numerical simulation of polymer injection in turbulent flow past a circular cylinder, J. Fluids Eng. **133**, 104501 (2011).
[7] T. Vaithianathan, A. Robert, J. G. Brasseur, and L. R. Collins, Polymer mixing in shear-driven turbulence, J. Fluid Mech. **585**, 487 (2007).
[8] M. C. Guimarães, N. Pimentel, F. T. Pinho, and C. B. da Silva, Direct numerical simulations of turbulent viscoelastic jets, J. Fluid Mech. **899**, A11 (2020).
[9] M. C. Guimarães, F. T. Pinho, and C. B. da Silva, Turbulent planar wakes of viscoelastic fluids analysed by direct numerical simulations, J. Fluid Mech. **946**, A26 (2022).
[10] M. C. Guimarães, F. T. Pinho, and C. B. da Silva, The similarity theory of free turbulent shear flows of viscoelastic fluids, J. Non-Newtonian Fluid Mech. **323**, 105148 (2024).
[11] S. Yamani, Y. Raj, T. A. Zaki, G. H. McKinley, and I. Bischofberger, Spatiotemporal signatures of elastoinertial turbulence in viscoelastic planar jets, Phys. Rev. Fluids **8**, 064610 (2023).
[12] S. H. Peng, Y. B. Zhang, and H. D. Xi, Effects of polymer additives on the entrainment of turbulent water jet, Phys. Fluids **35**, 045110 (2023).
[13] P. K. Ray and T. A. Zaki, Absolute/convective instability of planar viscoelastic jets, Phys. Fluids **27**, 014110 (2015).

[14] M. C. Guimarães, F. T. Pinho, and C. B. da Silva, Viscoelastic jet instabilities studied by direct numerical simulations, Phys. Rev. Fluids **8**, 103301 (2023).
[15] P. C. Valente, C. B. da Silva, and F. T. Pinho, The effect of viscoelasticity on the turbulent kinetic cascade, J. Fluid Mech. **760**, 39 (2014).
[16] G. Soligo and M. E. Rosti, Non-Newtonian turbulent jets at low-Reynolds number, Int. J. Multiphase Flow **167**, 104546 (2023).
[17] S. Yamani, B. Keshavarz, Y. Raj, T. A. Zaki, G. H. McKinley, and I. Bischofberger, Spectral universality of elastoinertial turbulence, Phys. Rev. Lett. **127**, 074501 (2021).
[18] H. Abreu, F. T. Pinho, and C. B. da Silva, Turbulent entrainment in viscoelastic fluids, J. Fluid Mech. **934**, A36 (2022).
[19] K. Kim, C. F. Li, R. Sureshkumar, S. Balachandar, and R. J. Adrian, Effects of polymer stresses on eddy structures in drag-reduced turbulent channel flow, J. Fluid Mech. **584**, 281 (2007).
[20] K. Horiuti, K. Matsumoto, and K. Fujiwara, Remarkable drag reduction in non-affine viscoelastic turbulent flows, Phys. Fluids **25**, 015106 (2013).
[21] P. O. Ferreira, F. T. Pinho, and C. B. da Silva, Large-eddy simulations of forced isotropic turbulence with viscoelastic fluids described by the FENE-P model, Phys. Fluids **28**, 125104 (2016).
[22] J. Page and T. A. Zaki, The dynamics of spanwise vorticity perturbations in homogeneous viscoelastic shear flow, J. Fluid Mech. **777**, 327 (2015).
[23] G. E. Gadd, Turbulence damping and drag reduction produced by certain additives in water, Nature (London) **206**, 463 (1965).
[24] G. E. Gadd, Reduction of turbulent friction in liquids by dissolved additives, Nature (London) **212**, 874 (1966).
[25] A. White, Some observations on the flow characteristics of certain dilute macromolecular solutions, in *Viscous Drag Reduction*, edited by C. S. Wells (Springer, New York, 1969), pp. 297–311.
[26] A. White, Turbulence and drag reduction with polymer additives, Ph.D. thesis, Middlesex Polytechnic, 1972.
[27] J. Wu, Drag reduction in external flows of additive solutions, in *Viscous Drag Reduction*, edited by C. S. Wells (Springer, New York, 1969), pp. 331–350.
[28] Z. P. Shul'man, N. A. Pokryvailo, N. D. Kovalevskaya, and V. V. Kulebyakin, Measurement of the turbulent flow structure of submerged jets of polymer solutions, J. Eng. Phys. **25**, 1475 (1973).
[29] J. W. Hoyt, J. J. Taylor, and C. D. Runge, The structure of jets of water, and polymer solution in air, J. Fluid Mech. **63**, 635 (1974).
[30] L. G. R. Filipsson, J. H. T. Lagerstedt, and F. H. Bark, A note on the analogous behaviour of turbulent jets of dilute polymer solutions, and fibre suspensions, J. Non-Newtonian Fluid Mech. **3**, 97 (1977).
[31] H. Usui, Y. Sano, T. Kawata, and K. Sakai, Turbulent round jet submerged in dilute drag reducing polymer solutions, Technol. Rep. Yamaguchi University **2**, 399 (1980).
[32] A. Gyr, Effects of polymer additives on the large scale structure of a two-dimensional submerged jet, Appl. Sci. Res. **56**, 13 (1996).
[33] Y. Goren and J. F. Norbury, Turbulent flow of dilute aqueous polymer solutions, J. Basic Eng. **89**, 814 (1967).
[34] D. N. Jackley, Drag-reducing fluids in a free turbulent jet, Int. Shipbuilding Prog. **14**, 158 (1967).
[35] R. A. Pownall and K. M. Kiser, Rate of spread of jets of non-Newtonian fluids, Ind. Eng. Chem. Fund. **9**, 293 (1970).
[36] R. W. Serth and K. M. Kiser, The effect of turbulence on hot-film anemometer response in viscoelastic fluids, AIChE J. **16**, 163 (1970).
[37] D. A. White, Velocity measurements in axisymmetric jets of dilute polymer solutions, J. Fluid Mech. **28**, 195 (1967).
[38] S. J. Barker, Laser-Doppler measurements on a round turbulent jet in dilute polymer solutions, J. Fluid Mech. **60**, 721 (1973).
[39] N. S. Berman and H. Tan, Two-component laser Doppler velocimeter studies of submerged jets of dilute polymer solutions, AIChE J. **31**, 208 (1985).

[40] K. Koziol and P. Glowacki, Turbulent jets of dilute polymer solutions, J. Non-Newtonian Fluid Mech. **32**, 311 (1989).
[41] S. A. Vlasov, O. V. Isaeva, and V. N. Kalashnikov, Average and pulsation components of velocity in submerged jets of polymer solutions, J. Eng. Phys. **25**, 1483 (1973).
[42] R. B. Bird, P. J. Dotson, and N. L. Johnson, Polymer solution rheology based on a finitely extensible bead-spring chain model, J. Non-Newtonian Fluid Mech. **7**, 213 (1980).
[43] R. Sureshkumar, A. N. Beris, and R. A. Handler, Direct numerical simulation of the turbulent channel flow of a polymer solution, Phys. Fluids **9**, 743 (1997).
[44] C. B. da Silva, D. C. Lopes, and V. Raman, The effect of subgrid-scale models on the entrainment of a passive scalar in a turbulent planar jet, J. Turbul. **16**, 342 (2015).
[45] C. B. da Silva, The role of coherent structures in the control, and interscale interactions of round, plane, and coaxial jets, Ph.D. thesis, INPG, Grenoble, 2001.
[46] C. B. da Silva and O. Métais, On the influence of coherent structures upon interscale interactions in turbulent plane jets, J. Fluid Mech. **473**, 103 (2002).
[47] C. Canuto, M. Y. Hussaini, A. Quarteroni, and T. A. Zang, *Spectral Methods in Fluid Dynamics* (Springer-Verlag, Berlin, 1987).
[48] S. K. Lele, Compact finite difference schemes with spectral-like resolution, J. Comput. Phys. **103**, 16 (1992).
[49] J. H. Williamson, Low-storage Runge-Kutta schemes, J. Comput. Phys. **35**, 48 (1980).
[50] J. Kim and P. Moin, Application of a fractional-step method to incompressible Navier-Stokes equations, J. Comput. Phys. **59**, 308 (1985).
[51] T. Vaithianathan, A. Robert, J. G. Brasseur, and L. R. Collins, An improved algorithm for simulating three-dimensional, viscoelastic turbulence, J. Non-Newtonian Fluid Mech. **140**, 3 (2006).
[52] A. Kurganov and E. Tadmor, New high-resolution central schemes for nonlinear conservation laws and convection-diffusion equations, J. Comput. Phys. **160**, 241 (2000).
[53] B. P. Leonard, A stable and accurate convective modelling procedure based on quadratic upstream interpolation, Comput. Methods Appl. Mech. Eng. **19**, 59 (1979).
[54] C. B. da Silva and O. Métais, Vortex control of bifurcating jets: A numerical study, Phys. Fluids **14**, 3798 (2002).
[55] P. Freymuth, On transition in a separated laminar boundary layer, J. Fluid Mech. **25**, 683 (1966).
[56] E. Gutmark and C.-M. Ho, Preferred modes and the spreading rates of jets, Phys. Fluids **26**, 2932 (1983).
[57] F. O. Thomas and V. W. Goldschmidt, Structural characteristics of a developing turbulent planar jet, J. Fluid Mech. **163**, 227 (1986).
[58] R. V. Garcia, Barotropic waves in straight parallel flow with curved velocity profile, Tellus A **8**, 82 (1956).
[59] A. Michalke, On the inviscid instability of the hyperbolic tangent velocity profile, J. Fluid Mech. **19**, 543 (1964).
[60] A. Michalke, Survey on jet instability theory, Prog. Aerosp. Sci. **21**, 159 (1984).
[61] T. Watanabe, Y. Sakai, K. Nagata, Y. Ito, and T. Hayase, Enstrophy and passive scalar transport near the turbulent/non-turbulent interface in a turbulent planar jet flow, Phys. Fluids **26**, 105103 (2014).
[62] S. Stanley and S. Sarkar, Simulations of spatially developing two-dimensional shear layers and jets, Theor. Comput. Fluid Dyn. **9**, 121 (1997).
[63] S. Stanley and S. Sarkar, Influence of nozzle conditions and discrete forcing on turbulent planar jets, AIAA J. **38**, 1615 (2000).
[64] S. Stanley and S. Sarkar, A study of the flow-field evolution and mixing in a planar turbulent jet using direct numerical simulation, J. Fluid Mech. **450**, 377 (2002).
[65] F. T. Pinho, C. F. Li, B. A. Younis, and R. Sureshkumar, A low Reynolds number turbulence closure for viscoelastic fluids, J. Non-Newtonian Fluid Mech. **154**, 89 (2008).
[66] H. Schlichting and K. Gersten, *Boundary Layer Theory*, 9th ed. (Springer-Verlag, Berlin, Heidelberg, 2017).
[67] P. E. Dimotakis, Turbulent mixing, Annu. Rev. Fluid Mech. **37**, 329 (2005).
[68] E. Villermaux, Mixing versus stirring, Annu. Rev. Fluid Mech. **51**, 245 (2019).

[69] D. Buaria, M. P. Clay, K. R. Sreenivasan, and P. K. Yeung, Turbulence is an ineffective mixer when Schmidt numbers are large, Phys. Rev. Lett. **126**, 074501 (2021).
[70] W. R. Peltier and C. P. Caulfield, Mixing efficiency in stratified shear flows, Annu. Rev. Fluid Mech. **35**, 135 (2003).
[71] K. B. Winters and E. A. D'Asaro, Diascalar flux and the rate of fluid mixing, J. Fluid Mech. **317**, 179 (1996).
[72] S. Kumar and G. M. Homsy, Direct numerical simulation of hydrodynamic instabilities in two- and three-dimensional viscoelastic free shear layers, J. Non-Newtonian Fluid Mech. **83**, 249 (1999).
[73] L. W. B. Browne and R. A. Antonia, Measurements of turbulent Prandtl number in a plane jet, J. Heat Transfer **105**, 663 (1983).
[74] R. A. Antonia and L. W. B. Browne, Conventional and conditional Prandtl number in a turbulent plane wake, Int. J. Heat Mass Transfer **30**, 2023 (1987).
[75] A. Berajeklian and L. Mydlarski, Simultaneous velocity-temperature measurements in the heated wake of a cylinder with implications for the modeling of turbulent passive scalars, Phys. Fluids **23**, 055107 (2011).
[76] C. B. da Silva, J. C. R. Hunt, I. Eames, and J. Westerweel, Interfacial layers between regions of different turbulent intensity, Annu. Rev. Fluid Mech. **46**, 567 (2014).
[77] T. Silva and C. B. da Silva, The behaviour of the scalar gradient across the turbulent/non-turbulent interface in jets, Phys. Fluids **29**, 085106 (2017).
[78] A. J. Sarnecki, The turbulent boundary layer on a permeable surface, Ph.D. thesis, Cambridge University, 1959.
[79] D. Krug, J. Philip, and I. Marusic, Revisiting the law of the wake in wall turbulence, J. Fluid Mech. **811**, 421 (2017).
[80] M. C. Guimaraes, D. O. A. Cruz, and A. P. Silva Freire, Similarity laws for transpired turbulent flows subjected to pressure gradients, separation and wall heat transfer, Int. J. Heat Fluid Flow **78**, 108436 (2019).
[81] A. A. Townsend, The fully developed wake of a circular cylinder, Aust. J. Chem. **2**, 451 (1949).
[82] P. Freymuth and M. S. Uberoi, Structure of temperature fluctuations in the turbulent wake behind a heated cylinder, Phys. Fluids **14**, 2574 (1971).
[83] J. C. LaRue and P. A. Libby, Temperature fluctuations in the plane turbulent wake, Phys. Fluids **17**, 1956 (1974).
[84] G. Fabris, Conditional sampling study of the turbulent wake of a cylinder. Part 1, J. Fluid Mech. **94**, 673 (1979).
[85] R. A. Antonia and L. W. B. Browne, Heat transport in a turbulent plane wake, Int. J. Heat Mass Transfer **29**, 1585 (1986).
[86] L. W. B. Browne and R. A. Antonia, Reynolds shear stress and heat flux measurements in a cylinder wake, Phys. Fluids **29**, 709 (1986).
[87] H. Rehab, R. A. Antonia, and L. Djenidi, Streamwise evolution of a high-Schmidt-number passive scalar in a turbulent plane wake, Exp. Fluids **31**, 186 (2001).
[88] H. Kang and C. Meneveau, Universality of large eddy simulation parameters across a turbulent wake behind a heated cylinder, J. Turbul. **3**, N32 (2002).
[89] J. Mi, Y. Zhou, and G. J. Nathan, The effect of Reynolds number on the passive scalar field in the turbulent wake of a circular cylinder, Flow, Turbul. Combust. **72**, 311 (2004).
[90] B. G. Van Der Hegge Zijnen, Measurements of turbulence in a plane jet of air by the diffusion method and by the hot-wire method, Appl. Sci. Res., Sect. A **7**, 293 (1958).
[91] P. E. Jenkins and V. W. Goldschmidt, Mean temperature and velocity in a plane turbulent jet, ASME: J. Fluids Eng. **95**, 581 (1973).
[92] R. A. Antonia, L. W. B. Browne, A. J. Chambers, and S. Rajagopalan, Budget of the temperature variance in a turbulent plane jet, Int. J. Heat Mass Transfer **26**, 41 (1983).
[93] R. Ramaprian and M. S. Chandrasekhara, LDA measurements in plane turbulent jets, ASME J. Fluids Eng. **107**, 264 (1985).
[94] T. Watanabe, Y. Sakai, K. Nagata, and O. Terashima, Experimental study on the reaction rate of a second-order chemical reaction in a planar liquid jet, AIChE J. **60**, 3969 (2014).

[95] O. Terashima, Y. Sakai, and Y. Ito, Measurement of fluctuating temperature and POD analysis of eigenmodes in a heated planar jet, Exp. Therm. Fluid Sci. **92**, 113 (2018).

[96] N. Wu, Y. Sakai, K. Nagata, Y. Ito, O. Terashima, and T. Hayase, Influence of Reynolds number on coherent structure, flow transition, and evolution of the plane jet, J. Fluid Sci. Technol. **9**, JFST0013 (2014).